



A Wolf 359 in Sheep’s Clothing: Hunting for Substellar Companions in the Fifth-closest System Using Combined High-contrast Imaging and Radial Velocity Analysis

Rachel Bowens-Rubin¹ , Joseph M. Akana Murphy^{1,11} , Philip M. Hinz¹ , Mary Anne Limbach² , Andreas Seifahrt³ , Rocio Kiman^{4,5} , Maïssa Salama¹ , Sagnick Mukherjee¹ , Madison Brady³ , Aarynn L. Carter¹ , Rebecca Jensen-Clem¹ , Maaïke A. M. van Kooten⁶ , Howard Isaacson^{7,8} , Molly Kosiarek¹ , Jacob L. Bean³ , David Kasper³ , Rafael Luque³ , Gudmundur Stefánsson⁹ , and Julian Stürmer^{10,12}

¹ Astronomy Department, University of California Santa Cruz, 1156 High Street, Santa Cruz, CA 95064, USA; rbowru@ucsc.edu

² Department of Astronomy, University of Michigan, Ann Arbor, MI 48109, USA

³ Department of Astronomy & Astrophysics, University of Chicago, 5640 South Ellis Avenue, Chicago, IL 60637, USA

⁴ Department of Astronomy, California Institute of Technology, Pasadena, CA 91125, USA

⁵ Kavli Institute for Theoretical Physics, University of California Santa Barbara, Kohn Hall, Santa Barbara, CA 93106, USA

⁶ Herzberg Astronomy and Astrophysics Research Centre, 5071 West Saanich Road, Victoria, BC, V9E 2E7, Canada

⁷ Department of Astronomy, University of California, Berkeley, CA 94720, USA

⁸ Centre for Astrophysics, University of Southern Queensland, Toowoomba, QLD, Australia

⁹ Department of Astrophysical Sciences, Princeton University, 4 Ivy Lane, Princeton, NJ 08540, USA

¹⁰ Landessternwarte, Zentrum für Astronomie der Universität Heidelberg, Königstuhl 12, D-69117 Heidelberg, Germany

Received 2023 May 19; revised 2023 September 6; accepted 2023 September 26; published 2023 November 22

Abstract

Wolf 359 (CN Leo, GJ 406, Gaia DR3 3864972938605115520) is a low-mass star in the fifth-closest neighboring system (2.41 pc). Because of its relative youth and proximity, Wolf 359 offers a unique opportunity to study substellar companions around M stars using infrared high-contrast imaging and radial velocity monitoring. We present the results of *Ms*-band (4.67 μm) vector vortex coronagraphic imaging using Keck-NIRC2 and add 12 Keck-HIRES and 68 MAROON-X velocities to the radial velocity baseline. Our analysis incorporates these data alongside literature radial velocities from CARMENES, the High Accuracy Radial velocity Planet Searcher, and Keck-HIRES to rule out the existence of a close ($a < 10$ au) stellar or brown dwarf companion and the majority of large gas giant companions. Our survey does not refute or confirm the long-period radial velocity candidate, Wolf 359 b ($P \sim 2900$ days), but rules out the candidate’s existence as a large gas giant ($>4 M_{\text{Jup}}$) assuming an age of younger than 1 Gyr. We discuss the performance of our high-contrast imaging survey to aid future observers using Keck-NIRC2 in conjunction with the vortex coronagraph in the *Ms* band and conclude by exploring the direct imaging capabilities with JWST to observe Jupiter- and Neptune-mass planets around Wolf 359.

Unified Astronomy Thesaurus concepts: [Coronagraphic imaging \(313\)](#); [Direct imaging \(387\)](#); [M stars \(985\)](#); [Radial velocity \(1332\)](#); [Exoplanets \(498\)](#); [Cold Neptunes \(2132\)](#)

Supporting material: machine-readable tables

1. Introduction

Over 70% of the stars in our galaxy are M dwarfs, yet we know little about the exoplanets that exist in these systems beyond the snow line ($\gtrsim 0.5$ au; Mulders et al. 2015). Most exoplanet detection methods and surveys are blind to this discovery space. The geometric probability of an exoplanet transit occurring for an exoplanet orbiting an M dwarf beyond 1 au is less than 0.1%. Astrometry and radial velocity (RV) surveys of M dwarfs require lengthy baselines in order to observe a planet’s full orbit because planets orbiting low-mass stars have longer periods for an equivalent separation.

Microlensing surveys have provided the first hint that cold gas giants, ice giants, and super-Earths could be common outside the snow line of M dwarfs with an increasing prevalence for smaller planets. A survey from Cassan et al. (2012) estimated that the

majority of low-mass stars host a giant planet between 0.5 and 10 au, with Jupiter-like planets ($0.3\text{--}10 M_{\text{Jup}}$) at an occurrence rate of $17^{+6}_{-9}\%$, Neptune-like planets ($10\text{--}30 M_{\oplus}$) at a rate of $52^{+22}_{-29}\%$, and super-Earths ($5\text{--}10 M_{\oplus}$) at a rate of $62^{+35}_{-37}\%$. A microlensing survey by the Microlensing Observations in Astrophysics collaboration is consistent with these results and concluded that Neptune-sized planets are one of the most common types of planet seen outside the snow line (Suzuki et al. 2016). Poleski et al. (2021) used data from the Optical Gravitational Lensing Experiment to determine that nearly every star could host an ice giant planet from 5 to 15 au, measuring an occurrence rate of $1.4^{+0.9}_{-0.6}$ ice giants per system.

Exoplanet direct imaging—where photons from an exoplanet are spatially resolved from their host star—is the only exoplanet detection technique that offers a pathway for characterizing the atmosphere, composition, and formation history for exoplanets orbiting beyond the snow line that are unlikely to transit. When directly imaging the closest set of stellar neighbors ($d < 5$ pc), the current generation of high-contrast imaging (HCI) systems on 8–10 m telescopes can probe comparatively colder planets at angular separations corresponding to where the prevalence of exoplanets outside the snow line is expected to peak (1–10 au; Fernandes et al. 2019). Proximity in stellar distance makes

¹¹ NSF Graduate Research Fellow.

¹² NASA Sagan Fellow.



companions appear at proportionally wider separation angles from their host star for a given orbit ($\theta_{\text{sep}} \propto a/d$) and boosts the apparent magnitude of the companion logarithmically ($m = 5 \log_{10}(d/10 \text{ pc}) + M$). This makes companions that are dimmer in absolute magnitude and closer in orbital separation easier to detect than if they were in a more distant analogous system.

The heritage of detecting exoplanets via the direct imaging technique has been to conduct blind surveys of hundreds of young star systems in search of a rare set of large gas giant planets on long-period orbits that are bright enough to detect using short integration times. Thanks to the growing abundance of long-baseline exoplanet RV data (e.g., Trifonov et al. 2020; Rosenthal et al. 2021; Ribas et al. 2023), we can now use RV data in tandem with HCI observations to tailor our imaging observations to conduct lengthier measurements around fewer systems. Information from RV data can be applied to select viable targets for imaging, choose the optimal imaging filters, predict how much integration time is required, and predict when a companion will be at its maximum separation from its host star. This targeted approach to HCI observing motivates the use of extended observing sequences that can expand our abilities to directly image colder ($<500 \text{ K}$) companions.

In many cases, we only need a hint of a companion’s existence to curate an HCI observation using RV data. Cheetham et al. (2018) demonstrated this by leveraging RV data to directly image an ultracool brown dwarf, HD 4113C. Based on the CORALIE survey’s detection of long-term RV trends (Udry et al. 2000), Rickman et al. (2019) conducted targeted direct imaging resulting in the discovery of three giant planets and two brown dwarfs. The TRENDS HCI survey used long-baseline velocities from the W. M. Keck Observatory High Resolution Echelle Spectrometer (Keck-HIRES) to target their survey for white dwarf and substellar companions (e.g., Crepp et al. 2016, 2018). Hinkley et al. (2023) used the VLTI/GRAVITY instrument to discover HD 206893 c by utilizing long-baseline RV data from the European Southern Observatory’s High Accuracy Radial velocity Planet Searcher (HARPS; Pepe et al. 2002; Mayor et al. 2003) and correlating it with the Gaia-Hipparcos astrometry accelerations (Brandt 2021) and orbital astrometry of the system’s outer companion.

Conducting targeted HCI observations of nearby systems that span multiple nights is becoming an increasingly common observing strategy to probe for sub-Jupiter-mass exoplanets. The surveys from Mawet et al. (2019) and Llop-Sayson et al. (2021) completed multnight HCI campaigns of the nearby, youthful ε Eridani system ($d = 3.22 \text{ pc}$, age = $600 \pm 200 \text{ Myr}$) with the goal of directly detecting the RV-discovered exoplanet, ε Eridani b. Combined, the 2017 and 2019 surveys collected nearly 16 hr of $4.67 \mu\text{m}$ imaging data over 9 nights using the W. M. Keck Observatory’s NIRC2 Imager (Keck-NIRC2; Wizinowich et al. 2000) but were not able to make an imaging detection of the planet. By combining the mass upper limits from HCI with RV and Gaia accelerations, Llop-Sayson et al. (2021) constrained the mass of ε Eridani b to be in the sub-Jupiter-mass domain, $0.66_{-0.09}^{+0.12} M_{\text{Jup}}$. Wagner et al. (2021) also demonstrated the advantage of searching for companions around nearby stars by performing a 100 hr HCI survey at $10\text{--}12.5 \mu\text{m}$ of the α Centauri system ($d = 1.3 \text{ pc}$, age = $5.3 \pm 0.3 \text{ Gyr}$). They imaged one candidate and demonstrated that it was possible to achieve survey sensitivities down to warm sub-Neptune-mass planets through the majority of the α Centauri habitable zone. While these surveys were not

able to make definitive direct detections, they demonstrated the possibilities of future ground-based mid-infrared HCI campaigns of nearby stars.

In this paper, we present the results of our joint HCI–RV survey to search for substellar companions around the solar-neighborhood star Wolf 359 (CN Leo, GJ 406, Gaia DR3 3864972938605115520). The paper is organized as follows. In the remainder of Section 1, we provide an overview of the Wolf 359 system. In Section 2, we report our observational and data reduction methods for the Keck-NIRC2 coronagraphic imaging survey and the RV measurements from Keck-HIRES (Vogt et al. 1994) and the Gemini-North MAROON-X spectrograph (Seifahrt et al. 2020). In Section 3, we estimate Wolf 359’s stellar age, apply these age constraints to the HCI data to set companion mass upper bounds, and provide an updated RV analysis combining our measurements with the previously published RV data from HARPS, Keck-HIRES, and CARMENES. In Section 4, we discuss how our imaging performance with Keck-NIRC2 compared to the predicted performance and then explore what JWST HCI could reveal about the Wolf 359 system.

1.1. The Wolf 359 System

Wolf 359 is a solar-metallicity M6V star (Pineda et al. 2021) and one of our nearest stellar neighbors¹³ (2.41 pc ; Gaia Collaboration et al. 2023). Table 1 summarizes Wolf 359’s stellar parameters.

RV surveys have been monitoring Wolf 359 for more than two decades. A preprint paper presented by Tuomi et al. (2019) identified two exoplanet candidates orbiting Wolf 359 using 63 RV measurements from Keck-HIRES and HARPS spanning 13 yr. These planet candidates are summarized in Table 2. The shorter-period candidate (Wolf 359 c) was refuted by Lafarga et al. (2021) after determining that the RV signal matched the star’s rotation period. The RV signal for the Wolf 359 b candidate could correspond to a cold, Neptune-like exoplanet on a wide orbit of approximately 8 yr ($P_{\text{orb}} = 2938 \pm 436 \text{ days}$, $a = 1.845_{-0.258}^{+0.289} \text{ au}$; Tuomi et al. 2019).

Wolf 359 has conflicting age estimates in the literature, but most indicate that the star is young ($<1 \text{ Gyr}$). The star is highly active, with stellar flares that occur approximately once every 2 hr (Lin et al. 2022). Wolf 359 has strong flare activity even among flaring M dwarfs (Lin et al. 2021), which is consistent with a youthful age estimate. An age estimate by Pavlenko et al. (2006) made by modeling the spectral energy distribution predicts that Wolf 359 could be as young as 100–350 Myr, which is consistent with its high activity. Wolf 359 also has a fast rotation period ($P_{\text{rot}} = 2.705 \pm 0.007 \text{ days}$; Guinan & Engle 2018), as confirmed with photometry from K2 (Howell et al. 2014), among other observatories. The combination of the gyrochronological relationship from Engle & Guinan (2018) and Wolf 359’s stellar rotation period suggests an age estimate of $<500 \text{ Myr}$. However, the star lies at the edge of Engle & Guinan’s (2018) rotation–activity–age relationship for M0–6 stars, and the rotation period cannot act as a direct proxy for age in this system in this context.

¹³ As one of our nearest neighbors, this system has captured the public’s interest and is a setting in many fictional stories, including the Wolf 359 podcast (<https://wolf359.fm/>) and several episodes in the *Star Trek* franchise.

Table 1
Properties of Wolf 359

Property	Value
R.A. J2000	10 56 28.92 ^a
Decl. J2000	+07 00 53.00 ^a
Distance	2.4086 ± 0.0004 pc ^a
Parallax	415.18 ± 0.07 mas ^a
Spectral type	Solar-metallicity M6 ^b
Mass	0.110 ± 0.003 M _☉ ^c
T _{eff}	2749 ⁺⁴⁴ ₋₄₁ K ^c
Radius	0.144 ± 0.004 M _☉ ^c
log(g)	5.5 cgs ^d
V mag	13.5 ^e
R mag	11.684 ^e
H mag	6.482 ^f
MKO <i>Ms</i> mag	5.85 ± 0.06 ^g
Rotation period	2.705 ± 0.007 days ^h
Age range	100 Myr–1.5 Gyr ⁱ

Notes.

^a Gaia Collaboration et al. (2023).

^b Kesseli et al. (2019).

^c Pineda et al. (2021).

^d Fuhrmeister et al. (2005).

^e Landolt (2009).

^f Cutri et al. (2003).

^g Leggett et al. (2010).

^h Guinan & Engle (2018).

ⁱ The lower estimate is from Pavlenko et al. (2006), and the upper estimate is from the kinematic age estimated in Section 3.1 of this work.

The combination of Wolf 359’s proximity and potential youth make it an ideal system for searching for companions using infrared direct imaging. An exoplanet candidate like Wolf 359 b would not be possible to directly image around most star systems. However, because Wolf 359 is one of our nearest neighbors, the parameters of the Wolf 359 b candidate can be constrained using our current generation of HCI instruments operating at 8–10 m telescopes.

2. Observations and Data Reduction

2.1. Keck II NIRC2 Vortex Coronagraphy

We conducted HCI observations of the Wolf 359 system with the W. M. Keck Observatory NIRC2 imager coupled with the vector vortex coronagraph (Serabyn et al. 2017). We completed our observations over 3 nights, as summarized in Table 3.

We conducted HCI observations using the fixedhex pupil stop with Keck’s *L/M*-band vortex coronagraph. The telescope was operated in the vertical angle rotation mode (sky PA = 4°43) to enable angular differential imaging (ADI) analysis methods. The centering of the vortex was controlled using the in-house QACTIS IDL software package (Huby et al. 2017). Each QACTIS sequence consisted of a set of (1) three calibration images to acquire an off-axis star point-spread function (PSF) and sky images, (2) three optimization images to center the star on the vortex and stabilize the tip/tilt in the adaptive optics (AO) system, and (3) a series of science images.

We operated the Keck II AO system with the recently commissioned near-infrared pyramid wave-front sensor (PyWFS; Bond et al. 2020) in natural guide star mode. We

selected the PyWFS over the facility Shack–Hartmann wave-front sensor because it is better suited for performing AO corrections when using an M dwarf as a natural guide star because it operates in the *H* band (1.633 μm, NIRC2 filters¹⁴) rather than the *R* band (0.641 μm; Bessell 2005). Wolf 359 is 5.2 mag brighter in the *H* band versus *R* band (Cutri et al. 2003; Landolt 2009); thus, we were able to take advantage of the improved AO quality with the significantly more flux available for wave-front correction.

Our HCI survey spanned 3 nights in 2021: February 22, February 23, and March 31 (UT). We collected images using the *Ms* filter (4.670 μm, NIRC2 filters; see footnote 14) with NIRC2 operated in narrow mode. The science images had a frame size of 512 × 512 pixels (5″090 × 5″090; pixel scale = 0″00942 ± 0″00005 pixel⁻¹, Keck General Specs¹⁶). The frames were taken with an integration time of 0.3 s with 90 coadds. We obtained a total of 664 science frames over 14 QACTIS sequences, totaling 4.98 hr of science integration time.

We performed our data reduction using the Vortex Imaging Processing (VIP) python package (Gomez Gonzalez et al. 2017). We preprocessed the NIRC2 data for bad pixels, flat-field correction, and sky background correction using the automated pipeline described in Xuan et al. (2018) using VIP version 0.9.9. Sky subtraction was completed using the principal component analysis (PCA)–based approach described in Hunziker et al. (2018) using VIP version 1.3.0. After preprocessing the science images, we removed 5% of the lowest-quality science frames using VIP’s Pearson correlation bad-frame detection from each night.

To establish an anchor for our reported contrast, we measured the flux of Wolf 359 using the unobstructed PSF images taken at the start of the QACTIS sequence. We created a PSF template by combining and then normalizing the 14 PSF images taken on 2021 March 31 (UT). The PSF frames were collected using an integration time per coadd of 0.015 s with 100 coadds. We performed the stellar photometry using the `fit_2dgaussian` function, as outlined in the VIP tutorial. We measured the FWHM of the NIRC2 *Ms* PSF to be FWHM = 9.67 pixel (0″0962).

We created the final reduced image using the combined image set from the 3 nights with the 631 images that passed bad-frame detection. We applied a high-pass filter to each individual image using VIP’s Gaussian high-pass filter with size 2.25 FWHM. The images were then derotated using the parallactic angle and median combined. We subtracted the stellar PSF using full-frame ADI PCA using VIP’s `pca` module (following the methods of Amara & Quanz 2012 and Soummer et al. 2012). We performed PCA optimization by injecting a fake companion 100 pixels from the star to determine the number of principal components that yielded the maximum signal-to-noise ratio (S/N) of the fake companion. The 3 night combined image set had an optimal number of principal components of PC = 18 (PC = 4 when high-pass filtering was applied). While performing PCA stellar point-spread subtraction, we adopted a center masking of 2 FWHM and a parallactic exclusion angle the size of 1 FWHM. The final reduced image from the high-pass-filtered 3 night combined image set is shown in Figure 1 along with its

¹⁴ <https://www2.keck.hawaii.edu/inst/nirc2/filters.html>

¹⁶ https://www2.keck.hawaii.edu/inst/nirc2/nirc2_snr_eff.html

¹⁵ <https://www2.keck.hawaii.edu/inst/nirc2/genspecs.html>

Table 2
Exoplanet Candidates Identified by Tuomi et al. (2019)

Candidate	Period (days)	$m \sin i (M_{\oplus})$	a (au)	Status	Note
Wolf 359 b	2938 ± 436	$43.9^{+29.5}_{-23.9}$	$1.845^{+0.289}_{-0.258}$	Possible cold Neptune	Investigated in this work
Wolf 359 c	$2.6869^{+0.0004}_{-0.0003}$	$3.8^{+2.0}_{-1.6}$	0.018 ± 0.002	False positive ^a	RV signal is due to star rotation

Note.

^a Wolf 359 c was refuted by Lafarga et al. (2021).

Table 3
HCI Keck-NIRC2 Observing Summary

Date (UT)	Total Sci. Frames	Total Int. Time (hr)	PA Change	PWV Opacity	Optimal PC Full fr. PCA	$5\sigma\Delta\text{Mag } 0''.2$ (0.5 au)	$5\sigma\Delta\text{Mag } 0''.98$ (1 au)	$5\sigma\Delta\text{Mag } 1''.7$ (4 au)
2021 Feb 22	181	1.36	77°35	0.08–0.20	8	6.0	7.3	7.5
2021 Feb 23	200	1.50	76°88	0.06–0.10	28	6.1	7.5	8.3
2021 Mar 31	283	2.12	126°29	0.10–0.16	14	6.4	7.7	8.6
Combined nights	664	4.98	18	6.8	8.2	8.9

Note. All science images were collected using the MKO M_s filter, tint = 0.3 s, coadd = 90, and subframe size = 512×512 with NIRC2 in narrow mode. The precipitable water vapor opacity was measured at 225 GHz by the Submillimeter Array and retrieved at <http://www.eao.hawaii.edu/weather/opacity/mk/archive/>. The optimal PC and 5σ contrast is reported for the image sets with no high-pass filter applied. To convert the listed ΔMag to MKO M_s apparent magnitude, add 5.85.

accompanying S/N threshold map. We detected no point-source signals above a 2σ threshold using VIP’s built-in detection function in log mode. We thus conclude that we did not detect any companions in the direct imaging portion of this survey.

We created contrast curves using VIP’s `contrast_curve` function, which calculates the $\sigma * \text{noise}/\text{throughput}$ using fake planet injection with a Student t-distribution correction. We found that applying a high-pass filter had little effect on our final sensitivity, so our contrast curves are reported using the images with no applied high-pass filtering. The combined-nights contrast curve was calculated by first processing the sensitivity by separation for each night separately. The combined-nights sensitivity was then calculated using a weighted variance at each separation, $\sigma_{\text{comb}}(\text{sep}) = \sqrt{1/(\sigma_{n1}(\text{sep})^{-2} + \sigma_{n2}(\text{sep})^{-2} + \sigma_{n3}(\text{sep})^{-2})}$. The overall sensitivity of the HCI survey of Wolf 359 is plotted in Figure 2.

2.2. RV Observations

2.2.1. Keck-HIRES

We present an additional 12 Keck-HIRES high-precision RV measurements gathered by the California Planet Search (CPS) team between 2017 December 25 and 2022 January 13 (UT). The Keck-HIRES velocities are available in Appendix A and online in machine-readable format. These measurements extend the baseline of the Keck-HIRES post-2004 velocities to over 17 yr when combined with the 40 Keck-HIRES RVs included in Tuomi et al. (2019). The new Keck-HIRES exposures were collected with the C2 decker ($14'' \times 0''.86$, $R = 45,000$) and had a median integration time of 1800 s, corresponding to a median S/N of 65 pixel^{-1} at 5500 \AA .

Observations were taken with a warm (50°C) cell of molecular iodine at the entrance slit (Butler et al. 1996), and RVs were determined following the procedures of Howard et al. (2010). The superposition of the iodine absorption lines

on the stellar spectrum provides both a fiducial wavelength solution and a precise, observation-specific characterization of the instrument’s PSF. Each RV spectrum was then modeled as the product of the deconvolved template spectrum and the Fourier Transform Spectrograph molecular iodine spectrum, which is convolved with the PSF. The χ^2 value of this model is minimized with the RV (Z) as one of the free parameters.

RVs computed via the iodine cell method require a high-S/N, iodine-free “template” of the stellar spectrum. Ideally, CPS aims for template spectra to have an S/N of about 200 pixel^{-1} at 5500 \AA in order to properly deconvolve the spectrum with the instrument’s PSF, which is measured by observing rapidly rotating B stars immediately before and after the template exposure(s). In the case of Wolf 359, CPS acquired three consecutive iodine-free exposures of the star on 2005 February 27 with the B1 decker ($3''.5 \times 0''.574$, $R = 60,000$). Each observation had an exposure time of 400 s corresponding to a combined S/N of 40 pixel^{-1} at 5500 \AA . Because Wolf 359 is relatively faint in the V band ($V = 13.5 \text{ mag}$; Landolt 2009), high-S/N Keck-HIRES exposures quickly become prohibitively expensive (an S/N of $\sim 100 \text{ pixel}^{-1}$ would take well over an hour of integration). Rather than attempt to acquire another, higher-S/N template of Wolf 359, we searched for a best-match template from a library of over 300 stars with high-S/N, iodine-free Keck-HIRES spectra and bracketing B star observations following the methods of Dalba et al. (2020). Recomputing the RVs using the best-match template that we identified increased the RV errors by a factor of ~ 2 , so we chose to continue to use the original CPS template. The poor match might be a consequence of Wolf 359’s late spectral type; the library from Dalba et al. (2020) contains stars with $T_{\text{eff}} > 3000 \text{ K}$. Using the CPS template, RVs taken before the Keck-HIRES detector upgrade in 2004 have a median measurement error of 8.2 m s^{-1} , and post-upgrade RVs have a median measurement error of 3.9 m s^{-1} .

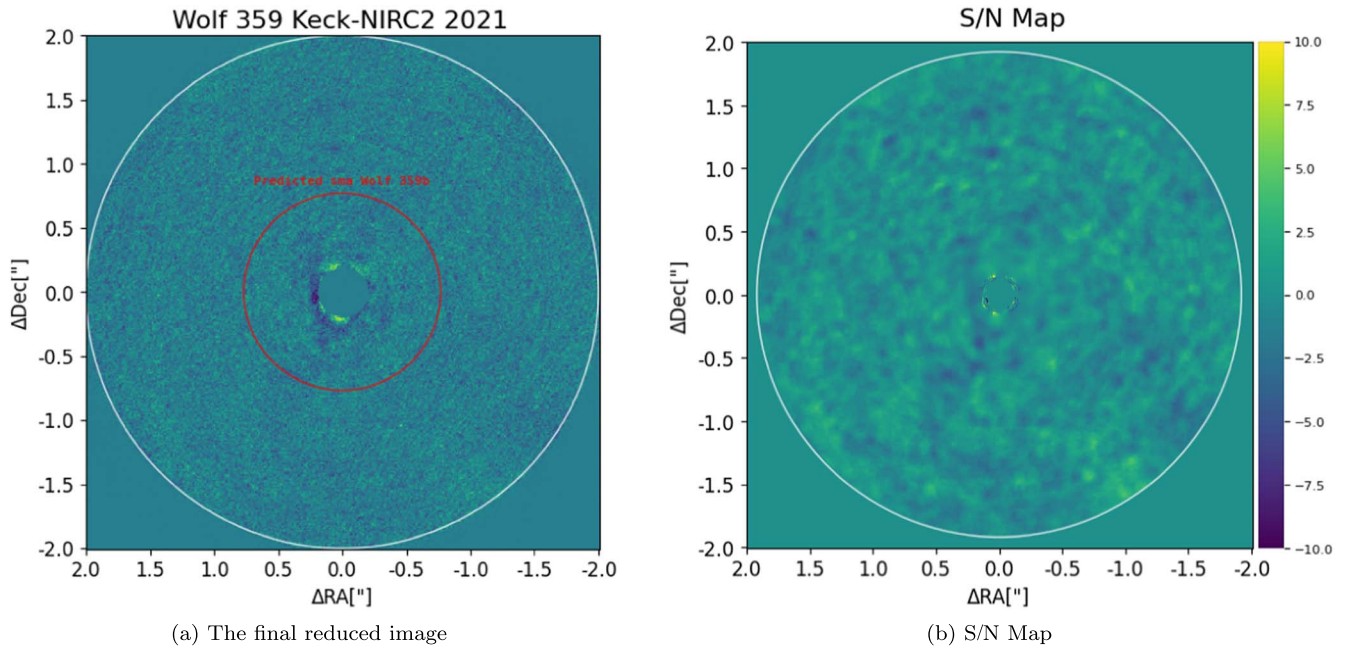


Figure 1. Final reduced image of the Wolf 359 system from the Keck-NIRC2 HCI survey. Our final reduced image of the Wolf 359 system was created using the high-pass-filtered 3 night combined image cube. The corresponding S/N map is shown in panel (b). The red circle shown in panel (a) corresponds to the predicted semimajor axis of the Wolf 359 b candidate. The stellar PSF was subtracted using full-frame PCA with VIP. No companion-like point sources were detected to more than 2σ above the background using VIP’s built-in detection function.

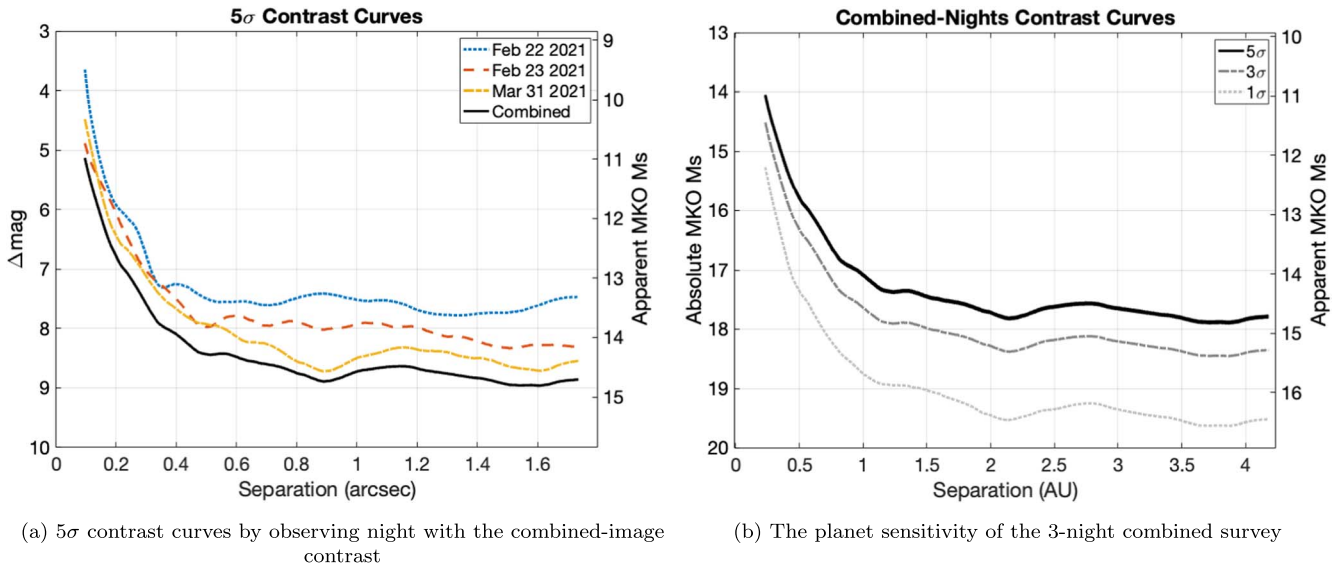


Figure 2. Contrast curves from the Keck-NIRC2 imaging survey. The contrast curves were created using the full-frame PCA algorithm in VIP with the images that were not high-pass filtered. The solid black line represents the 5σ sensitivity achieved with the combined-nights cube.

2.2.2. MAROON-X

We publish 68 measurements of Wolf 359 made with the MAROON-X spectrograph at Gemini Observatory. The MAROON-X velocities are available in Appendix A and online in machine-readable format. The MAROON-X data were acquired with both the red (649–920 nm) and blue (491–670 nm) arms simultaneously during 34 observing nights. These observations were taken over five observing runs during 2021 February, 2021 April, 2021 May, 2021 November, and 2022 April.

Spectra were taken with a fixed exposure time of 30 minutes and showed an average peak S/N of 90 pixel^{-1} in the blue arm and 460 pixel^{-1} in the red arm. The data were reduced by the

instrument team using a custom `python3` data reduction pipeline to produce optimum extracted and wavelength-calibrated 1D spectra. The RV analysis was performed using `SERVAL` (Zechmeister et al. 2018), a template-matching RV retrieval code in a custom `python3` implementation. On average, the RV uncertainty per datum was 1.0 m s^{-1} for the blue arm and 0.3 m s^{-1} for the red arm. MAROON-X uses a stabilized Fabry–Perot etalon for wavelength and drift calibration (Seifahrt et al. 2022) and can deliver 30 cm s^{-1} on-sky RV precision over short timescales (Trifonov et al. 2021) but suffers from inter-run RV offsets with additional per-epoch uncertainties ranging from 0.5 to 1.5 m s^{-1} , corresponding to increased uncertainties of

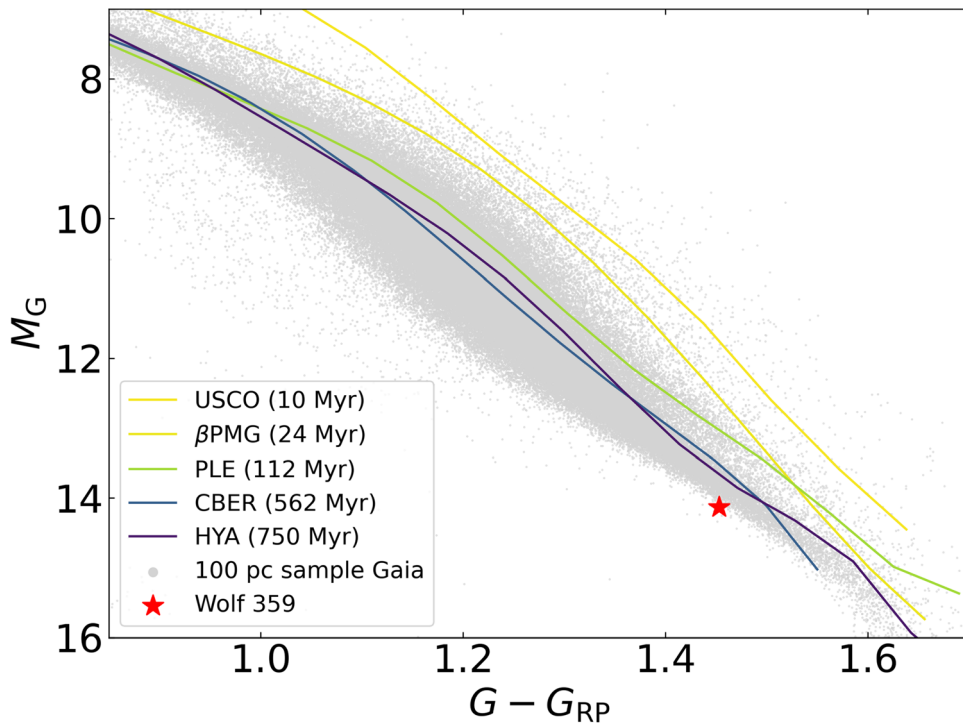


Figure 3. CMD comparison with young moving groups. We plot the CMD for Wolf 359 with empirical sequences from young associations of ages 10, 24, 112, 562, and 750 Myr (Gagné et al. 2021) and the Gaia 100 pc sample of M dwarfs. The red star represents the position of Wolf 359. The color–magnitude position of Wolf 359 is not in agreement with the youngest moving groups of 10–112 Myr. We find that Wolf 359 is in better agreement with the Coma Berenices (562 Myr) and Hyades (750 Myr) moving groups and the field sample. We conclude that Wolf 359 has converged onto the main sequence and that its age is older than 112 Myr.

1.4 m s^{-1} for the blue arm and 0.9 m s^{-1} for the red arm for signals on timescales longer than 1 month.

3. Analysis

3.1. Stellar Age Estimation

We provide an updated analysis of the age of Wolf 359 in order to constrain the sensitivities of our HCI survey. We correlate our age estimates to our HCI survey sensitivity using evolutionary cooling models in order to determine the maximum mass of an unseen companion in Section 3.2.

Gyrochronology. The relation between rotation period, age, and mass has been studied extensively for low-mass stars (e.g., Skumanich 1972; Barnes & Kim 2010; Irwin et al. 2011; Curtis et al. 2020). It has been shown that stars begin their life with a fast rotation period and spin down with time via magnetic braking. The particular shape of this relation and the time it takes a star to spin down depend on its mass. The gyrochronology relation for Sun-like stars is calibrated, so the rotation period can be used to estimate an age. However, this gyrochronology relationship for Sun-like stars does not hold for M dwarfs (e.g., Angus et al. 2019). While the relationship for low-mass stars has not been calibrated, it has been shown that rotation correlates with relative maturity (e.g., Popinchalk et al. 2021; Dungee et al. 2022; Pass et al. 2022).

We calculated Wolf 359’s Rossby number to be $R_0 = 0.02$ using the convective turnover time computed from Wright et al. (2011). We then compared our R_0 value to Figure 6 in Newton et al. (2017). We find that Wolf 359 lies in the magnetically saturated portion of this plot. For Sun-like stars, being in the saturated regime means the star is young (< 100 Myr). However, M dwarfs stay fast-rotating longer; thus, a fast

rotation period does not always mean the star is young (e.g., Irwin et al. 2011; Medina et al. 2022). Recently, Medina et al. (2022) estimated that fully convective M dwarfs transition between the saturated and unsaturated regimes at around 2.4 ± 0.3 Gyr, which provides an approximate upper limit to the age of Wolf 359 but is not informative. Below, we combine the rotation period with kinematics to estimate a more constrained upper limit on the age of Wolf 359.

CMD age dating. We compared the color–magnitude diagram (CMD) position of Wolf 359 against the 100 pc sample of M dwarfs from Gaia and empirical sequences based on bona fide members of young associations of several ages (Gagné et al. 2021). From Figure 3, we conclude that Wolf 359 has already converged into the main sequence. This analysis suggests that Wolf 359 is older than the age of the Pleiades cluster (112 Myr), as the lowest-mass stars in this cluster have not converged into the main sequence. From the CMD analysis, we conclude that the age of Wolf 359 is older than 112 Myr.

Isochrone age dating. We used the MESA Isochrones and Stellar Tracks (MIST; Choi et al. 2016; Dotter 2016) to estimate Wolf 359’s age using a CMD. We adopt the MESA models associated with an M6 star ($0.11 M_\odot$) with a metallicity of $[\text{Fe}/\text{H}] = 0.25$ dex (Mann et al. 2015) and rotation of $0.4v/v_{\text{crit}}$. We used Gaia photometry (apparent magnitude $g = 11.038 \pm 0.003$, absolute magnitude $G = 14.130 \pm 0.003$, apparent magnitude $g_{\text{bp}} = 13.770 \pm 0.005$) to compare with the MIST isochrones (Figure 4). Our isochrone age estimate is largely driven by the measurement of the Gaia G magnitude.

While the MIST models can be unreliable for low-mass stars, they were recently shown to provide a good fit for stars like Wolf 359 with masses below $0.25 M_\odot$ and a metallicity of $[\text{Fe}/\text{H}] = +0.25$ using the Hyades single star sequence

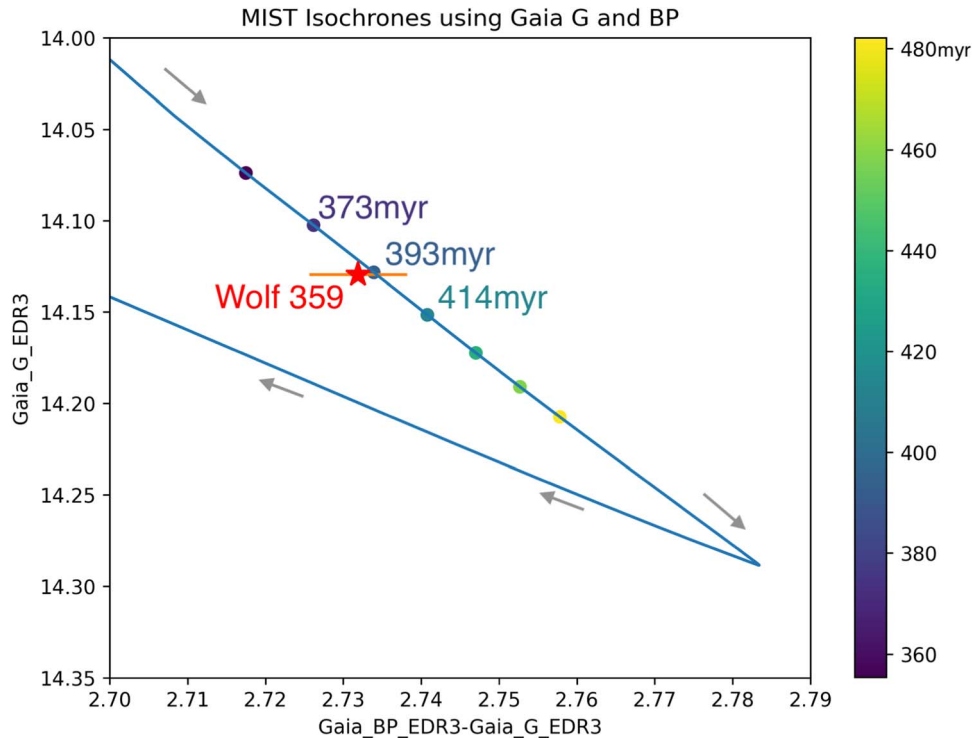


Figure 4. Isochrone age dating. We used the MIST isochrone models with the Gaia eDR3 photometry in G and BP to estimate an age for Wolf 359. The blue line represents the MIST isochrone track for a star of $0.11 M_{\odot}$ with a metallicity of $[Fe/H] = +0.25$ dex. Wolf 359 is represented by the red star, which lies closest to the isochrone point with an age of 393 Myr (between 373 and 414 Myr). We estimate an age of 400 Myr from isochrone dating.

(Brandner et al. 2023). We predict an age of ~ 400 Myr using the MIST models.

Kinematic age dating. We estimated Wolf 359’s kinematic age to be 1.53 ± 0.3 Gyr following the methods outlined in Lu et al. (2021). Briefly, this method consists of estimating the vertical velocity dispersion of a group of stars with similar temperatures and rotation periods. Assuming that the evolution of the rotation period for stars with similar temperatures is the same, the stars in this group should have similar ages. Therefore, we can use an age–velocity relation to estimate the average age of the group from the vertical velocity dispersion. We obtained a group of stars with similar mass and rotation period as Wolf 359 from the MEarth sample in Newton et al. (2018). We combined their reported rotation periods, masses, and RVs with their proper motions and parallaxes retrieved from Gaia eDR3 (Gaia Collaboration et al. 2021) in *galpy* (Bovy 2015)¹⁷ to calculate their vertical velocities. We then created a bin in mass and rotation period around Wolf 359, selecting similar stars with similar ages. To define the size of the bin, we used a group of stars with similar mass and rotation period as one M dwarf in the MEarth sample that is comoving with a white dwarf. We used *wdwarfdate* (Kiman et al. 2022) to get the age of the white dwarf from its effective temperature and surface gravity (retrieved from Gentile Fusillo et al. 2021) and set the bin size so that the kinematic age of the group reproduced that age. We used the age–velocity relation from Yu & Liu (2018) to correlate the vertical velocity dispersion with age and then performed a Monte Carlo propagation of the vertical velocity uncertainties to determine the uncertainty in the kinematic age of Wolf 359. The resulting distribution from the Monte Carlo simulation is shown in

Figure 5. We obtained a kinematic age of 1.5 ± 0.3 Gyr. However, as most of the stars in the bin are in the saturated regime, their rotation period still depends on their initial rotation period, making the dispersion in age larger. Therefore, we adopt an age of 1.5 Gyr as an upper bound for Wolf 359’s age.

Age summary. Our age estimate from the MIST isochrone comparison (400 Myr) is consistent with our young association comparison (>112 Myr). Our CMD comparison with young moving groups shows it is probable that Wolf 359 has converged onto the main sequence. While the 2.7 day rotation period cannot be used to provide an exact age using gyrochronology, Wolf 359’s fast rotation is a relative indicator of youth (<2.4 Gyr). We provide a better-constrained upper bound estimate using the kinematic age dating of $\sim 1.5 \pm 0.3$ Gyr.

For completeness through the remainder of this paper, we consider ages for Wolf 359 between 100 Myr and 1.5 Gyr in our HCI analysis. However, our analysis suggests that the ages estimated by Pavlenko et al. (2006) using the spectral energy density distribution (~ 100 – 350 Myr) seem less likely due to Wolf 359’s suspected convergence with the main group. If we someday measure the dynamical mass and temperature of an exoplanet companion around Wolf 359 using infrared direct imaging, we may then be able to apply planetary-mass isochrones to refine this age estimate.

3.2. HCI Analysis

We used the Keck-NIRC2 contrast curves (Figure 2) to determine the final 5σ sensitivity of our imaging survey across separations between 0.23 and 4.18 au. We cannot make constraints on companions orbiting beyond separations of 4.18 au on the night of observation because the field of view of

¹⁷ Galpy: <https://github.com/jobovy/galpy>.

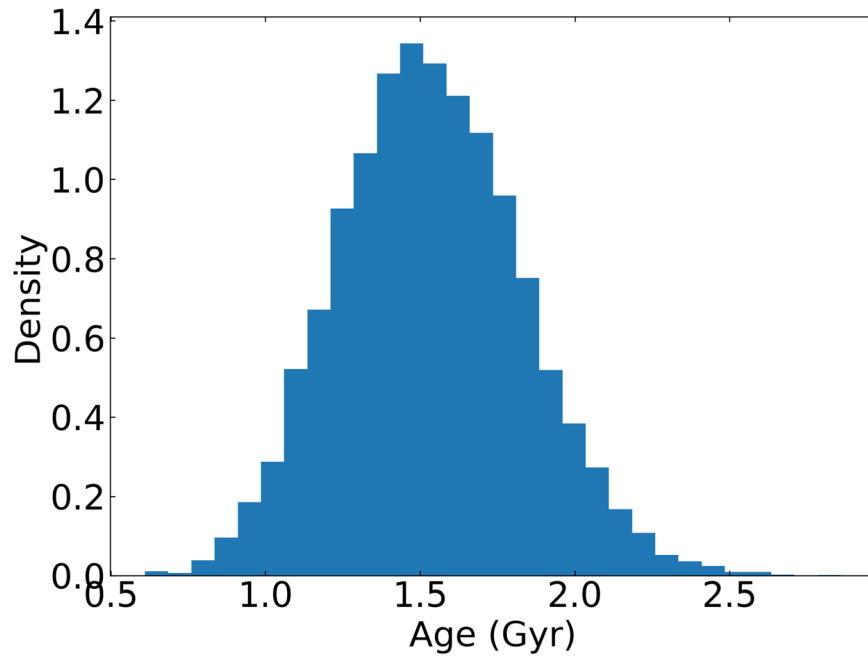
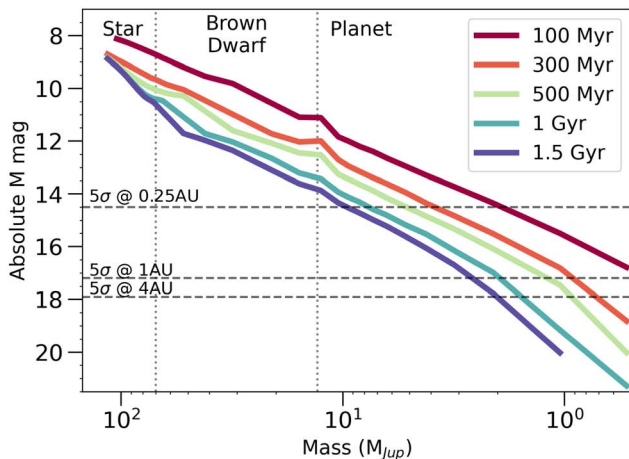
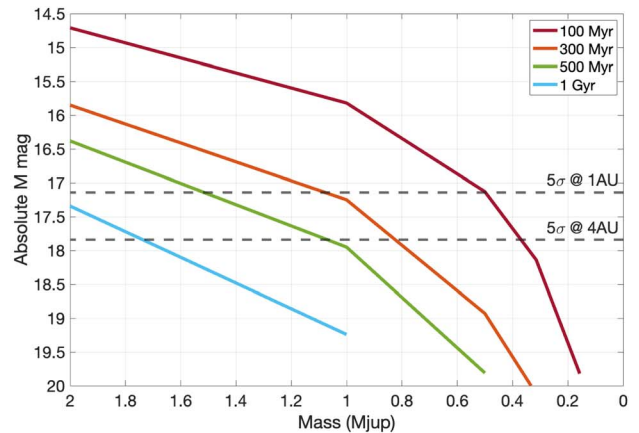


Figure 5. Kinematic age dating. Wolf 359’s kinematic age was measured using the methods outlined in Kiman et al. (2019). The results of the Monte Carlo simulation shown here find the kinematic age to be 1.53 ± 0.3 Gyr. We adopt this kinematic age as our age upper bound for Wolf 359.



(a) Baraffe Isochrones for stellar, brown dwarf, and planetary cooling regimes



(b) Linder+2019 low-mass planetary cooling curves

Figure 6. Isochrones overlaid with the 5σ constraints from the Keck-NIRC2 survey. The horizontal lines represent our imaging survey’s 5σ sensitivity at 1 and 4 au of separation. (a) We use the BHAC15/DUSTY/COND models (Chabrier et al. 2000; Baraffe et al. 2003, 2015) to rule out all tight stellar and brown dwarf companions ($>13 M_{\text{Jup}}$) outside of 0.25 au ($0''.1$). (b) From 1 to 4.18 au of separation, we apply the Linder et al. (2019) low-mass planetary cooling models to place upper mass limits on planetary companions. We rule out planets with masses $>1.5 M_{\text{Jup}}$ to 5σ if Wolf 359 is younger than 500 Myr in this region.

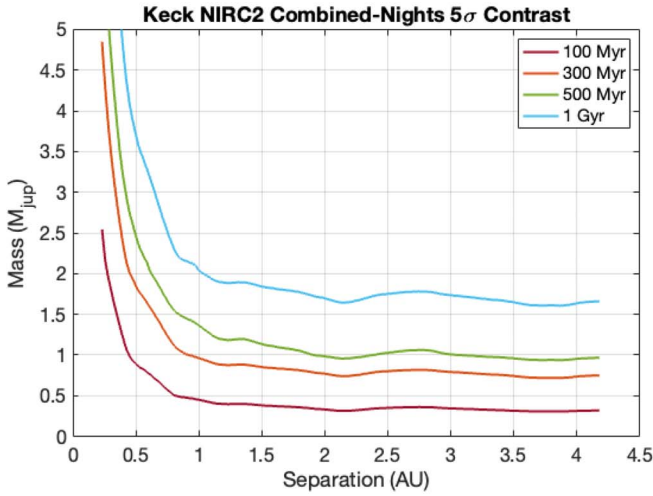
the camera was limited to $5''.1 \times 5''.1$ (512×512 pixel) to increase the speed of camera readout.

We then applied published isochrone models to predict the upper mass limits for companions ruled out by the HCI observations. In Figure 6(a), we apply the isochrone models created by Isabelle Baraffe¹⁸ to place constraints in the speckle-limited region at the tightest angular separations (<1 au). We used the BHAC15 models for the stellar regime ($T_{\text{eff}} > 3000$ K; Baraffe et al. 2015), the DUSTY models for the brown dwarf regime ($1700 \text{ K} < T_{\text{eff}} < 3000$ K; Chabrier et al. 2000), and the COND models for the planetary regime ($T_{\text{eff}} < 1400$ K;

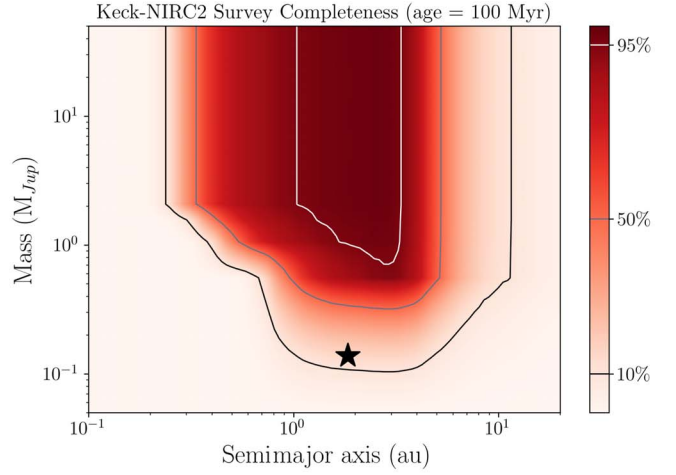
Baraffe et al. 2003). The Baraffe models predict that companions with masses above the deuterium-burning limit ($>13 M_{\text{Jup}}$) with ages younger than <1.5 Gyr will be brighter than $M_s = 14.0$. Our survey reached a greater than 5σ sensitivity to companions with $M_s = 14$ at separations greater than 0.25 au. We therefore rule out any stellar and brown dwarf companions orbiting outside of 0.25–4.18 au at the time of observation.

In Figure 6(b), we used the isochrone models presented by Linder et al. (2019) to set the mass upper limit in the background-limited regime from 1 to 4.18 au (Figure 6(b)), where the sensitivity is limited by the sky background rather than the stellar contrast. Our combined-nights contrast curve averages a sensitivity of $M_s = 17.7$ in this region.

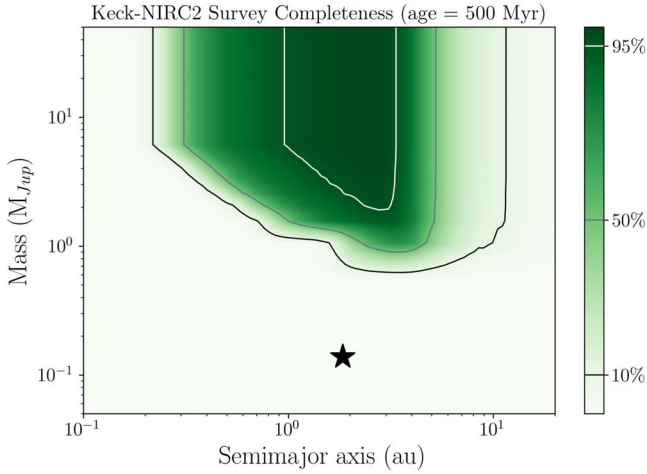
¹⁸ The Baraffe isochrone models were retrieved at <http://perso.ens-lyon.fr/isabelle.baraffe/>.



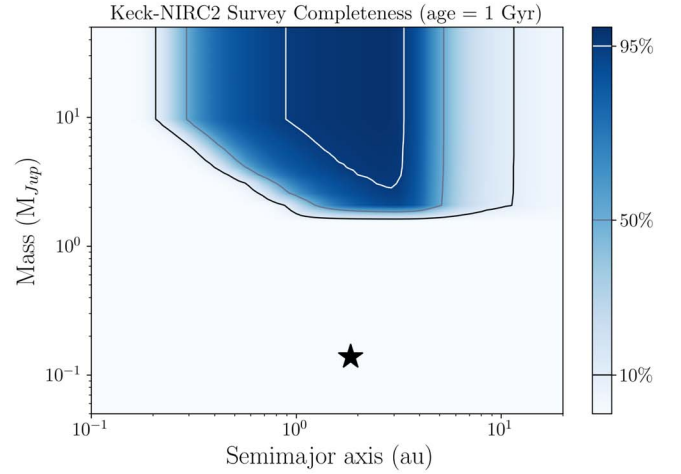
(a) Keck-NIRC2 combined-nights 5σ contrast curve in mass space for ages of 100 Myr, 300 Myr, 500 Myr, and 1 Gyr



(b) Completeness for an adopted age of 100 Myr



(c) Completeness for an adopted age of 500 Myr



(d) Completeness for an adopted age of 1 Gyr

Figure 7. Keck-NIRC2 HCI survey completeness. (a) The NIRC2 combined-nights 5σ contrast was converted to mass space using the Linder+2019 and Ames-COND isochrone models. (b)–(d) The NIRC2 survey completeness maps for ages of 100 Myr, 500 Myr, and 1 Gyr were estimated using the `EXO-DMC` python package from the mass-space combined-nights 5σ contrast curves. Our imaging survey has 10% coverage to companions with a semimajor axis of 0.2–10 au and reaches 95% coverage for companions with a semimajor axis between 1 and 3 au. The black star represents the Wolf 359 b semimajor axis and minimum mass as predicted by Tuomi et al. (2019).

This sensitivity rules out companions with a mass bigger than $2.1 M_{\text{Jup}}$ ($667 M_{\oplus}$) for ages younger than 1.5 Gyr. We cannot rule out companions to 5σ with masses smaller than $0.4 M_{\text{Jup}}$ ($127 M_{\oplus}$) for any adopted age older than 100 Myr.

In order to estimate the completeness by mass and orbital semimajor axis of the HCI survey, we utilized the Exoplanet Detection Map Calculator (`EXO-DMC`) python package (Bonavita 2020; Figure 7). We converted the combined-nights 5σ Keck-NIRC2 contrast curves from the apparent M mag into upper mass estimates adopting four ages: 100 Myr, 300 Myr, 500 Myr, and 1 Gyr (Figure 7(a)). We used the Linder and Ames-COND isochrone models for this conversion and averaged the estimated masses in areas where the models overlapped. The Ames-COND isochrones¹⁹ were accessed using the `species` python package (Stolker et al. 2020).

The 10% survey coverage spans a semimajor axis range of 0.2–10 au. We find the best survey coverage ($>95\%$) of the semimajor axis between 1 and 3 au. Assuming an age younger than 1 Gyr, we rule out companions with a semimajor axis of 1–3 au above $10 M_{\text{Jup}}$. While the semimajor axis predicted for the Wolf 359 b candidate ($a = 1.8 \pm 0.2$ au) is within this range, we do not reach the sensitivity to probe to the minimum mass predicted ($m \sin i \sim 0.14 M_{\text{Jup}}$) regardless of age. For an age of 1 Gyr, we rule out that the Wolf 359 b candidate as described by Tuomi et al. (2019) cannot be bigger than $4 M_{\text{Jup}}$. For an age of 100 Myr, we rule out that Wolf 359 b cannot be bigger than $1 M_{\text{Jup}}$.

3.3. RV Analysis

Our RV analysis incorporates 275 velocities from four instruments: Calar Alto Observatory’s CARMENES (Quirrenbach et al. 2016), ESO-HARPS (Mayor et al. 2003),

¹⁹ The Ames-COND models can be found at <https://phoenix.ens-lyon.fr/Grids/AMES-Cond/>.

Table 4
Wolf 359 RV Data Summary

Instrument	Source	Spectral Range (nm)	No. of Meas.	Baseline	Avg. RV Precision	Inst. Offset ^a
CARMENES	Retrieved from Ribas et al. (2023)	550–1700	78	2.23 yr	1.99 m s ⁻¹	0.05 m s ⁻¹
ESO-HARPS	Directly from M. Tuomi	378–691	77	15.3 yr	3.09 m s ⁻¹	-3.22 m s ⁻¹
HIRES pre-2004	CPS team	300–1000	14	5.05 yr	8.09 m s ⁻¹	-9.68 m s ⁻¹
HIRES post-2004	CPS team	300–1000	38	17.14 yr	4.26 m s ⁻¹	-3.28 m s ⁻¹
MAROON-X blue	MAROON-X team	499–663	34 ^b	1.17 yr	1.39 m s ⁻¹	-6.47 m s ⁻¹
MAROON-X red	MAROON-X team	649–920	34 ^b	1.17 yr	0.88 m s ⁻¹	-5.62 m s ⁻¹

Notes.

^a The instrument offsets were calculated from the fit made using *RVSearch* when detecting the signal from the stellar rotation period.

^b The MAROON-X blue and red data were collected simultaneously.

Keck-HIRES, and Gemini-MAROON-X. The RV instruments and measurements used in our analysis of Wolf 359 are summarized in Table 4 and available in full in machine-readable format online. The CARMENES data were retrieved from the DR1 release, which spans from 2016 to 2020 (Ribas et al. 2023). The MAROON-X, HIRES, and HARPS data were provided directly by the observing teams.

We elected to use the HARPS data as analyzed with the TERRA pipeline (Anglada-Escudé & Butler 2012) in order to remain consistent with the analysis presented in Tuomi et al. (2019). The 77 HARPS-TERRA velocities used in this analysis incorporate the velocities presented in the 2019 announcement.

The MAROON-X RVs were computed using both the red and blue arms of the spectrograph, producing two RV measurements per observation. We treat each of the MAROON-X red and blue arm measurements as being from different instruments to account for different instrumental offsets and RV jitter amplitudes. We do the same for the Keck-HIRES velocities collected before and after a detector upgrade in 2004. Within each instrument, we bin observations collected within 0.1 day of one another.

We used the *RVSearch*²⁰ python package (Rosenthal et al. 2021) to perform a blind planet search within our RV time series data (Figure 8). We detected the known signal associated with the rotation period of the star (2.71 days). Once the stellar rotation activity signal was removed, we detected no signals over a false-alarm probability of 0.1%. We used the injection-recovery tools built into *RVSearch* to estimate the sensitivity of our RV survey to planets of specified $m \sin i$ and semimajor axis to create the completeness contour shown in Figure 9. Figure 9 shows the probability of our analysis to recover an exoplanet with a minimum mass ($m \sin(i)$) of 17.2 Me (Neptune analog), 43.9 Me (Wolf 359b analog), and 317.8 (Jupiter analog). *RVSearch* yielded a 32% completeness to an equivalent $m \sin i$ and semimajor axis as the Wolf 359 b candidate. Because we do not have a significant completeness in this space, we are not able to confirm or deny the candidacy of Wolf 359 b using *RVSearch* with our RV data set.

To further explore the candidacy of Wolf 359 b, we used the open-source software package *radvel*²¹ (Fulton et al. 2018) to model the RV data. We used the Tuomi et al. (2019) results for Wolf 359 b listed in Table 2 as priors. We employed fits with and without the Gaussian process fitting module, which can be used to fit and remove signals due to stellar activity. We ran our *radvel* Markov Chain Monte Carlos using $N_{\text{walkers}} =$

50, $N_{\text{steps}} = 10000.0$, $N_{\text{ensembles}} = 6$, and Min Auto Factor = 30.0. In all *radvel* fits, the chains did not pass the convergence test to indicate that the walkers were well mixed. The convergence criteria could not be met, so we draw no conclusions about the properties of the Wolf 359 b candidate from our *radvel* fits.

We detected no new candidates. At 95% confidence, our RV analysis excludes planets with a minimum mass bigger than $m_p \sin i > 13.5 M_{\oplus}$ ($0.04 M_{\text{Jup}}$) for $a = 0.1$ au and $m_p \sin i > 147 M_{\oplus}$ ($0.46 M_{\text{Jup}}$) for $a = 1$ au. We have over 50% completeness to exclude planets with an $m_p \sin i$ equivalent to or bigger than $1 M_{\text{Jup}}$ within 5.3 au and 1 Neptune mass within 0.52 au. Our RV survey has little coverage of companions orbiting with a semimajor axis larger than $a > 10$ au for all masses.

4. Discussion

4.1. Performance of the Direct Imaging Survey with Keck-NIRC2

Few Keck-NIRC2 HCI observations have been published that span multiple nights that utilize the *Ms* filter (4.67 μm) in conjunction with the vector vortex coronagraph. Previous published deep surveys of this type have so far been limited to the ϵ Eri results from Mawet et al. (2019) and Llop-Sayson et al. (2021). However, it is expected that surveys similar to the work presented here will become more common as data from indirect methods of exoplanet detection become more widely available and drive targeted direct imaging surveys toward studying colder companions. We document the expected performance of our imaging survey as compared to our measured performance to aid in the planning of future multnight Keck-NIRC2 HCI surveys that are completed with the *Ms* filter with the vortex coronagraph.

We report that our measured efficiency on the night with the greatest number of images (2021 March 31 UT) was 52%. This excludes the setup time and used the observing configuration described in Section 2.1. After our initial setup, we observed Wolf 359 for 4.05 hr and totaled 2.12 hr of science integration time. We ran the majority of QACITS sequences with 50 science images (22.5 minutes total integration time) and experienced no significant QACITS centering issues while collecting science data.

We adopt the predictions produced by the Keck Observatory’s online NIRC2 S/N and efficiency calculator¹⁶ to quantify the expected S/N in the background-limited regime of our contrast curves. These equations for the NIRC2 S/N

²⁰ *RVSearch*: <https://github.com/California-Planet-Search/rvsearch>.

²¹ *Radvel*: <https://github.com/California-Planet-Search/radvel>.

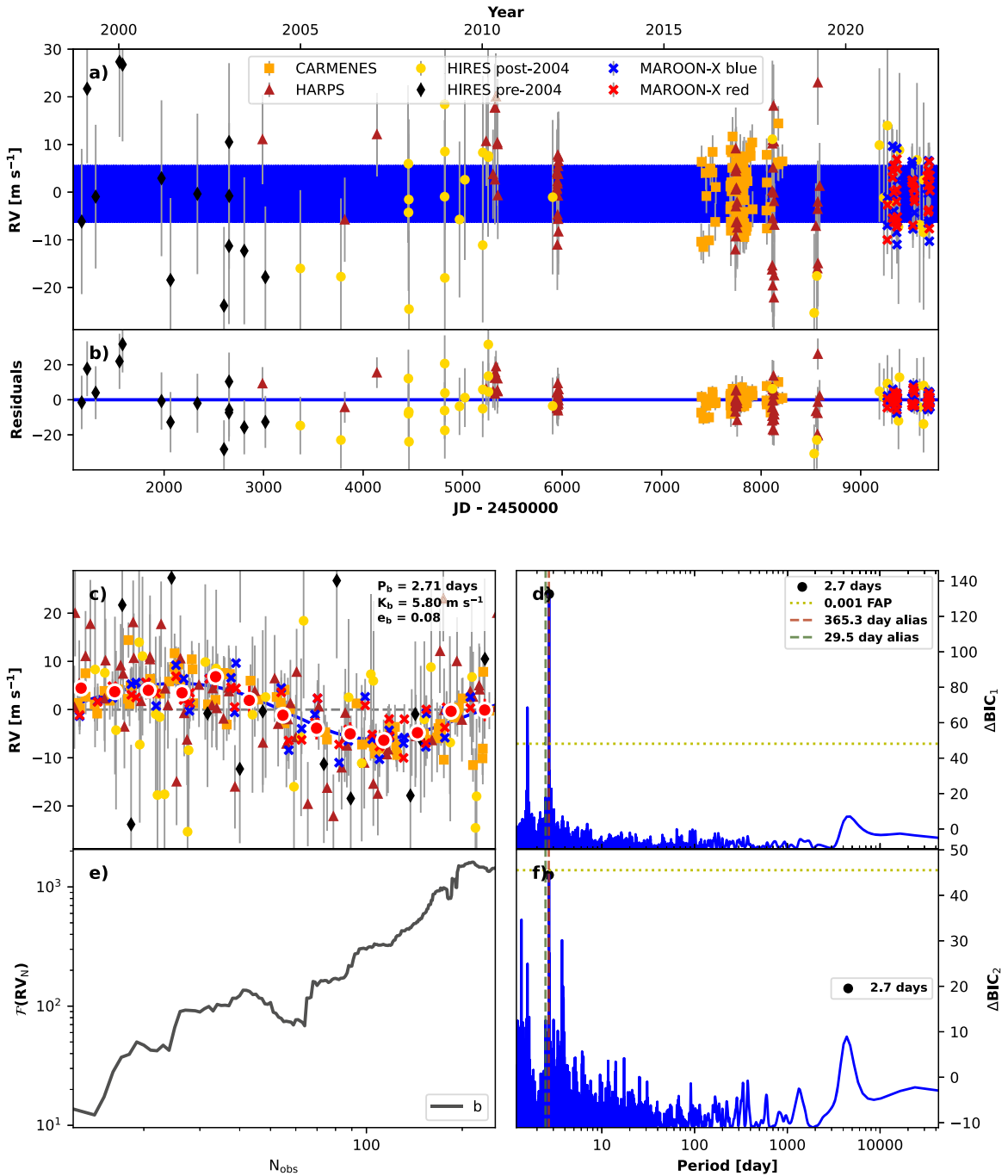


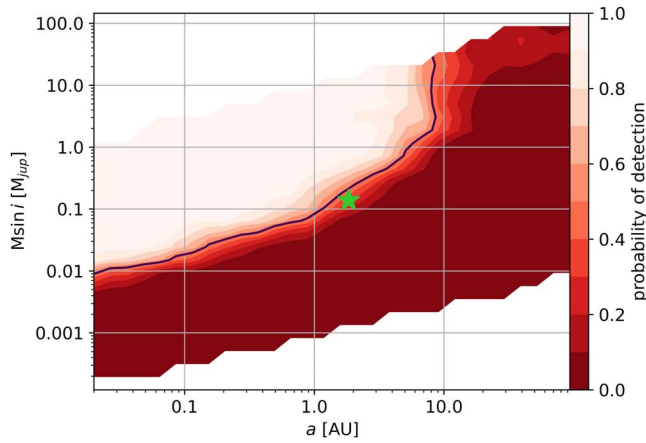
Figure 8. RV time series and periodograms from analysis using RVSearch. (a) We plot the RV time series using the available data from CARMENES, HARPS (TERRA pipeline), HIRES (pre- and post-2004), and MAROON-X (red and blue arms). The blue line represents the detected signal from the known rotation period (2.71 days; Guinan & Engle 2018). (b) The time series residuals after the stellar rotation activity signal is removed. (c) The folded time series for the rotation period signal. (d) The periodogram before removing the rotation period signal (2.71 days), and the second peak corresponds to half the rotation period (1.4 days). (e) We find that the quantification of the strength of the detection for the 2.7 day signal as a function of the number of observations monotonically increases as expected. (f) The periodogram of the residuals after removing the 2.71 day signal from the stellar rotation period. We do not find evidence of any additional candidates above our false-alarm probability threshold (0.1%). The local peak at 4370 days corresponds to a $\Delta\text{BIC} = 7.0$ (0.001 false-alarm probability corresponds to $\Delta\text{BIC} = 45.7$).

calculator are outlined in Appendix B. We do not consider the speckle-limited regime of our contrast curves from this comparison ($\text{sep} < 0''.8$), as the NIRC2 S/N calculator cannot quantify the S/N in the speckle-limited region.

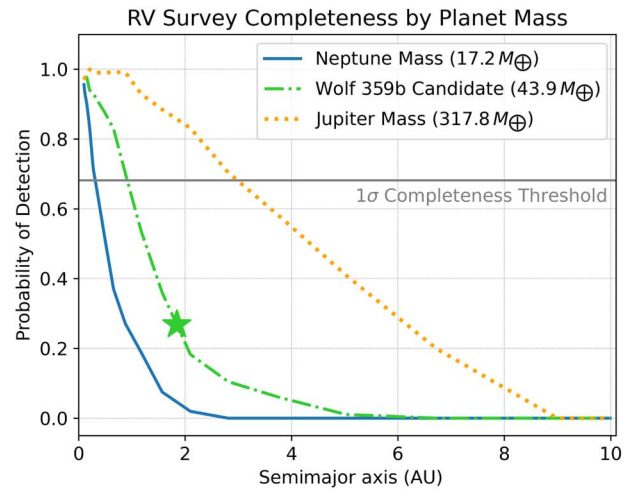
We evaluate the performance using 1 night of observations to avoid complications in the performance discussion from combining data across multiple nights. We elected to use 2021 March 31 (UT) because it is the night of our survey with the

most available data. Our contrast curve for this night was generated using 269 of the 283 images taken with an exposure time of 0.3 s and a coadd of 90, totaling approximately 2 hr of integration time. We measured an average 5σ contrast in the background-limited region of the contrast curve ($>0''.8$) to be $\Delta m_s = 8.53$ (apparent magnitude of $m_s = 14.38$).

Our measured 5σ detection limit from 2021 March 31 is consistent with the performance on individual nights of the ε



(a) Wolf 359 Radial Velocity Survey Completeness Contour



(b) Probability of Detection by Minimum Mass

Figure 9. RV survey completeness. We used the injection-recovery function within `RVSearch` to determine the completeness of our Wolf 359 RV survey as a function of the minimum planet mass and semimajor axis. Our analysis methods yield a 32% chance of recovering a signal that matched the Wolf 359 b candidate as described by Tuomi et al. (2019; green star).

Eri survey, where Llop-Sayson et al. (2021) used the PyWFS to collect approximately 2 hr of integration time. The best S/N achieved by Llop-Sayson et al. (2021) was between separations of $1''.5$ and $1''.75$ and corresponds to an apparent magnitude of $m_s = 14.4$ ($\Delta\text{mag} = 12.7$). Both this work and the ε Eri surveys indicate that it is improbable to detect a companion dimmer than $m_s = 14.4$ to 5σ with this instrument configuration in 1 half-night of Keck-NIRC2 time when operating with the vortex coronagraph paired with the PyWFS.

We next checked our measured results against the prediction made by the NIRC2 S/N calculator using the parameters that matched our observing setup: 0.3 s integration time with 90 coadds, narrow mode, two reads, 269 images, and no telescope nodding. We assumed a Strehl ratio of 0.85, which is a conservative estimate associated with 300 nm of wave-front error. The NIRC2 S/N calculator assumes that the background flux and the flux from the source will follow Poisson statistics. We find that the calculator predicts the 5σ threshold to be at an apparent magnitude of $m_s = 16.07$, which is not consistent with our observed results. Our measured S/N was 1.69 mag brighter than the predicted performance by the NIRC2 S/N calculator, meaning we were more restricted in the companions that we could detect at the background-limited wide separations than was predicted by the calculator.

We expect that the prediction by the NIRC2 calculator will be somewhat inconsistent with our results because the NIRC2 S/N calculator was not designed to predict observations when the vortex mask is used. To better refine our predicted performance estimate, we modified the equations used by the NIRC2 S/N calculator. These modifications are documented in Appendix B and incorporate a throughput penalty to the measured signal to account for the use of the fixhex pupil stop and the vortex mask at $4.7\ \mu\text{m}$ (total throughput penalty 0.57 ± 0.03). We additionally offer a revision to the background flux counts when the vortex is used in the M band ($17,850\ \text{DN s}^{-1}\ \text{pixel}^{-1}$). When we apply our revised equations to estimate the predicted performance for our 2021 March 31 data set, we find that our 5σ detection threshold is predicted to be at $m_s = 15.49$. While this estimate better aligns with our measured performance, this method still overestimates the

brightness of the 5σ detection threshold by 1.11 mag when comparing to our measured performance from that night ($m_s = 14.38$).

We ruled out the possibility that this performance gap was due to uncorrected nonuniform background counts spatially in the individual images through high-pass filtering. We used VIP’s internal high-pass filtering function to determine the optimal high-pass filtering by injecting a fake planet into each individual image, running six types of high-pass filters on each image, and then using stellar photometry to recover the S/N of the injected planet. The optimal high-pass filtering method was `gaussiansubt` with size $2.25 * \text{fwhm}_{\text{nirc2}}$. We then edited VIP’s contrast curve function to include the high-pass filtering step using the optimal high-pass filter. The high-pass filtering step was added after fake planet injection but before running PCA. There were slight differences between the contrast curves produced from the image sets with and without the high-pass filter, but the differences did not affect the contrast achievable in the background-limited region of the image. We thus conclude that the performance gap is not due to poorly corrected background structures in each frame.

To determine if the performance gap was due to the image background noise not temporally obeying the Poisson statistics, we measured how the sky background noise over time compared to the statistics expected from photon noise. We measured the sky background noise by summing the counts inside four circular apertures with a diameter equal to the $\text{fwhm}_{\text{NIRC2}}$ using the 2021 March 31 image set before and after sky subtraction was completed. The apertures were located $1''.76$ from the image center in the direction of the image corners in order to avoid contamination from the star. We found our measured background noise value using 20 frames from the image cube after the sky subtraction was applied. The 20 frames were chosen from the full cube where the conditions were stable (no background drift, average background counts in the raw frames are consistent, and similar AO correction). We plotted the aperture sum counts of each aperture and then took the standard deviation of the counts over time. The corresponding photon noise value was determined using the image cube before the background subtraction was made. We

measured the sum of the photons inside each aperture, averaged the sums, and then took the square root of the average sum to act as the expected photon noise. The ratio between our measured noise and photon noise contribution was 1.9 from the subset of the 20 stable frames. Across the full image cube, we found the ratio of measured/theoretical photon noise to be 3.0. This corresponds to a flux difference of 0.69 and 1.2 mag, respectively. This range of values is consistent with the performance gap we see after accounting for the throughput loss from the vortex and pupil stop ($\Delta\text{mag} = 1.1$).

We hypothesize that the background noise does not follow Poisson statistics because of short-timescale water vapor variations at timescales less than the length of our 30 s images. This hypothesis could be tested when upgrades to the NIRC2 electronics are completed in 2023, which will allow for faster readout and background corrections to be made at shorter timescales. If proven true, the limits of previous surveys may be improved upon by observing the target again using subsecond integration times in order to improve background correction.

4.2. Prospects for Directly Imaging an Exoplanet around Wolf 359 Using JWST

JWST offers an opportunity to directly image exoplanets in infrared wavelengths without contamination from the Earth’s atmosphere, allowing the telescope to probe for colder companions as compared to ground-based telescopes. In this section, we present simulations to explore the potential of JWST to directly image a cold giant planet orbiting Wolf 359 using the Near Infrared Camera (NIRCam) coronagraphic imaging mode and Mid-Infrared Instrument (MIRI) imaging. MIRI and NIRCam can be used in combination for wider coverage of companions in orbital separations, cloudiness, and temperature. NIRCam can be used to achieve high contrasts at subarcsecond inner working angles at shorter infrared wavelengths (0.6–5 μm ; Rieke et al. 2023), which was demonstrated successfully during the Early Release Science Program to image the super-Jupiter-mass exoplanet HIP 65426b (Carter et al. 2023). MIRI operates at longer infrared wavelengths (5–28 μm ; Wright et al. 2023), giving greater sensitivity to cold and cloudy companions.

Because of Wolf 359’s proximity, a planet revealed through NIRCam or MIRI imaging has the potential to become the coldest directly imaged exoplanet that could be characterized with JWST spectroscopy. If such an exoplanet is detected, detailed characterization would allow the planet to become an anchor to test theories related to the atmosphere and formation of cold gas giant and ice giant planets.

4.2.1. NIRCam Coronagraphic Imaging

We explore the possibilities of using the NIRCam coronagraphic imaging mode to directly image companions orbiting Wolf 359 by simulating contrast curves using the Pandemia Coronagraphy Advanced Kit for Extractions (PanCAKE) python package²² (Girard et al. 2018; Perrin et al. 2018; Carter et al. 2021). We considered observations in the F444W filter, as the broadest band between the 4 and 5 μm peak in brightness, in conjunction with the round coronagraphic mask MASK335R. We simulated integration times of 20 minutes,

1 hr, and 10 hr with ADI and reference-star differential imaging (RDI) subtraction techniques. To simulate the ADI contrast curve, we assumed that the total exposure time was split between two rolls (0° and 10°) when imaging the target. For the RDI simulations, we assumed a perfect reference with the same properties of Wolf 359 and used a nine-point circle dither pattern. PSFs were generated using the precomputed library over on-the-fly generation with wave-front evolution to reduce computational intensity. As such, these contrast curves represent an optimistic estimate of the achievable performance. We allowed PanCAKE to optimize the readout parameters for dither pattern, number of groups, and number of integrations.

To estimate what types of exoplanets may be detectable, we generated atmospheric models for companions with masses between $20 M_\oplus$ and $1 M_{\text{Jup}}$ for ages spanning 100 Myr–1.5 Gyr using the PICASO 3.0²³ (Batalha et al. 2019; Mukherjee et al. 2023) radiative–convective–thermochemical equilibrium model to simulate cloud-free 1D atmospheres for such companions. We assumed solar metallicity and a C/O ratio for our simulated atmospheres. To estimate the T_{eff} and radius of a companion with a given mass at a certain age, we used the Linder et al. (2019) evolutionary tracks and linearly extrapolated along the age axis when needed. The Phoenix stellar models (Husser et al. 2013) were employed to generate the stellar model for Wolf 359 using a spectral type of M5V and the Vega mag scaled to $2\text{MASS } k_s = 6.084$. An example of a set of thermal emission spectra from our generated atmospheric models is shown in Figure 10.

Our simulated NIRCam contrast curves are shown in Figure 11. Table 5 summarizes the detectability of theoretical cloudless exoplanets with varying masses using NIRCam in ADI mode with 1 hr of total integration time. While our simulations span from 1 to 7 au ($0''.4$ – $3''$), the full NIRCam field of view from the MASK335R inner working angle ($0''.57$) to $20''$ would correspond to 1.4–48.2 au. We estimate that the region from 7 to 48.2 au will be background-limited and have the same contrast as the result at 7 au for future observing planning purposes.

One hour of NIRCam integration time would provide sensitivity to a cloudless Jupiter-mass companion outside of $0''.62$ (1.5 au) at any predicted age range. Cloudless Saturn-mass exoplanets ($0.3 M_{\text{Jup}}$) would be detectable at small separations if Wolf 359 is in the youngest part of its age range and at wider background-limited separations for ages up to ~ 1 Gyr. A Neptune-like exoplanet ($17 M_\oplus$, $0.06 M_{\text{Jup}}$) will be visible if it is orbiting at wider separations and Wolf 359 is in the youngest part of its age range. The detection of a cloudless sub-Neptune exoplanet is unlikely with 1 hr NIRCam ADI at any separations within Wolf 359’s age range.

4.2.2. MIRI Imaging

Exoplanet gas giants with clear atmospheres are particularly bright in the emission band between 4 and 5 μm , often making them detectable by the JWST NIRCam instrument. However, gas giants with cloudier atmospheres have muted emission from 4 to 5 μm , instead emitting more at longer wavelengths ($>15 \mu\text{m}$), as illustrated in Figure 12. This figure shows the emission differences between a cloudy (solid lines) and clear (dashed lines) young sub-Saturn exoplanet ($0.12 M_{\text{Jup}}$). The

²² Pandemia Coronagraphy Advanced Kit for Extractions; <https://github.com/spacetelescope/pandemia-coronagraphy>.

²³ Planetary Intensity Code for Atmospheric Spectroscopy Observations, <https://github.com/natashabatalha/picaso>.

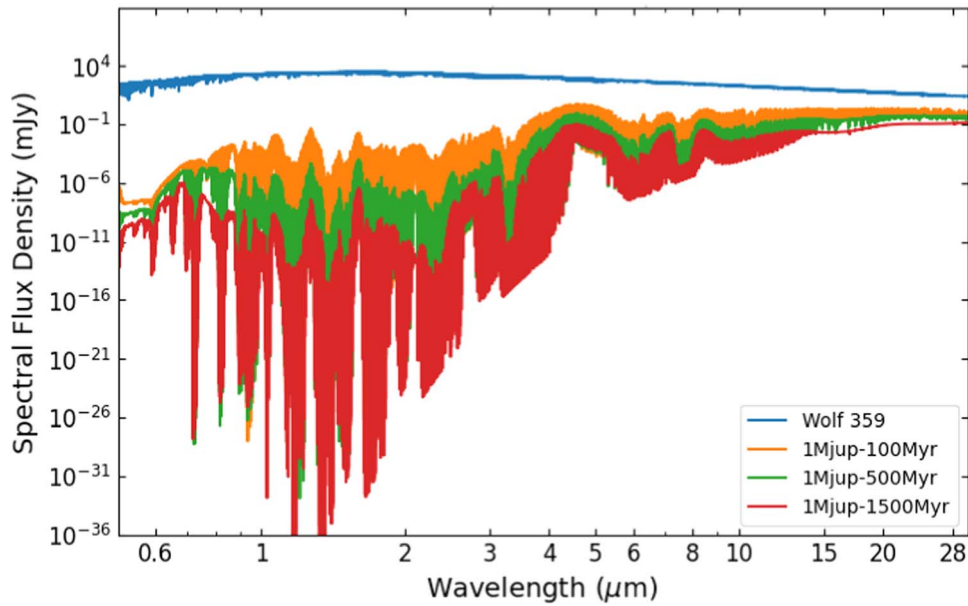


Figure 10. Simulated atmospheric models for Wolf 359 and a cloudless $1 M_{\text{Jup}}$ companion. The modeled companion spectra shown correspond to ages of 100 Myr (orange), 500 Myr (green), and 1.5 Gyr (red). The simulated spectrum of the Wolf 359 host star is shown in blue. The estimates of the flux between 3.881 and $4.982 \mu\text{m}$ were used to determine the expected brightness and S/N for each companion type to simulate a NIRCcam observation with F444W+MASK335R using PanCAKE.

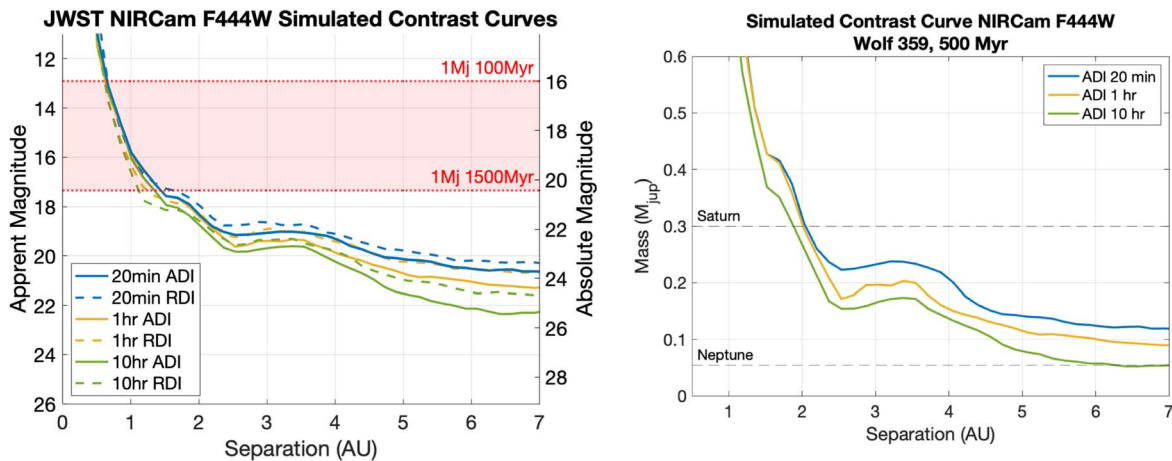


Figure 11. Simulated JWST NIRCcam coronagraphic imaging 5σ contrast curves with the F444W filter. (Left) We show contrast curves simulated using PanCAKE for three NIRCcam exposure times in ADI and RDI mode. We predict that if a cloudless exoplanet existed with a mass greater than $1 M_{\text{Jup}}$ outside of ~ 1.5 au, it would be detectable with 20 minutes of integration time. (Right) The NIRCcam F444W 5σ ADI contrast curves were converted to mass space using the Linder et al. (2019) models with an adopted age of 500 Myr. We find that exoplanets larger than 1 Saturn mass will be detectable outside of 2 au if Wolf 359 is in the younger part of its age range. A Neptune-mass planet will be detectable beyond 6 au if Wolf 359 is younger than 500 Myr and a >10 hr exposure is used.

cloudy and clear models used in this figure were generated using the method described in Limbach et al. (2022). This figure demonstrates that exoplanets with cloudy atmospheres may be more easily detected through JWST MIRI broadband imaging at $21 \mu\text{m}$, while clear atmospheres are more readily detected through direct imaging with NIRCcam at $4.5 \mu\text{m}$.

We briefly explore the possibility of imaging exoplanets, like the Wolf 359 b candidate from Tuomi et al. (2019), with MIRI. In the mid-IR, the planet’s emission is increasing, and the star’s emission is decreasing. This results in a favorable contrast ratio of the planet to the star of 1:1120 for an exoplanet that is 100 Myr, $0.12 M_{\text{Jup}}$ with moderate cloud cover ($f_{\text{SED}} = 2$). However, the diffraction limit of JWST at $21 \mu\text{m}$ is $0''.67$ (6 pixels), which is comparable to the separation between Wolf 359 b and the host star. Using the coronagraphic mask at $23 \mu\text{m}$, which has an inner working angle of $3.3\lambda/D$, would

block exoplanets at separations of $<2''16$. Therefore, we instead consider directly imaging the system without a coronagraph and using KLIP (Soummer et al. 2012) in postprocessing to recover the exoplanet. KLIP has the potential to improve the contrast by approximately $\sim 100\times$ (Rajan et al. 2015).

Figure 13 shows the simulated MIRI contrast curve. To create this simulation, we used the premade set of PSFs for JWST MIRI based on the in-flight optical performance WebbPSF tool.²⁴ We used the F21000W PSF that includes geometric optical distortions. The contrast curve for KLIP was calculated assuming performance similar to that described in Rajan et al. (2015).

²⁴ jwst-docs.stsci.edu/jwst-mid-infrared-instrument/miri-performance/miri-point-spread-functions

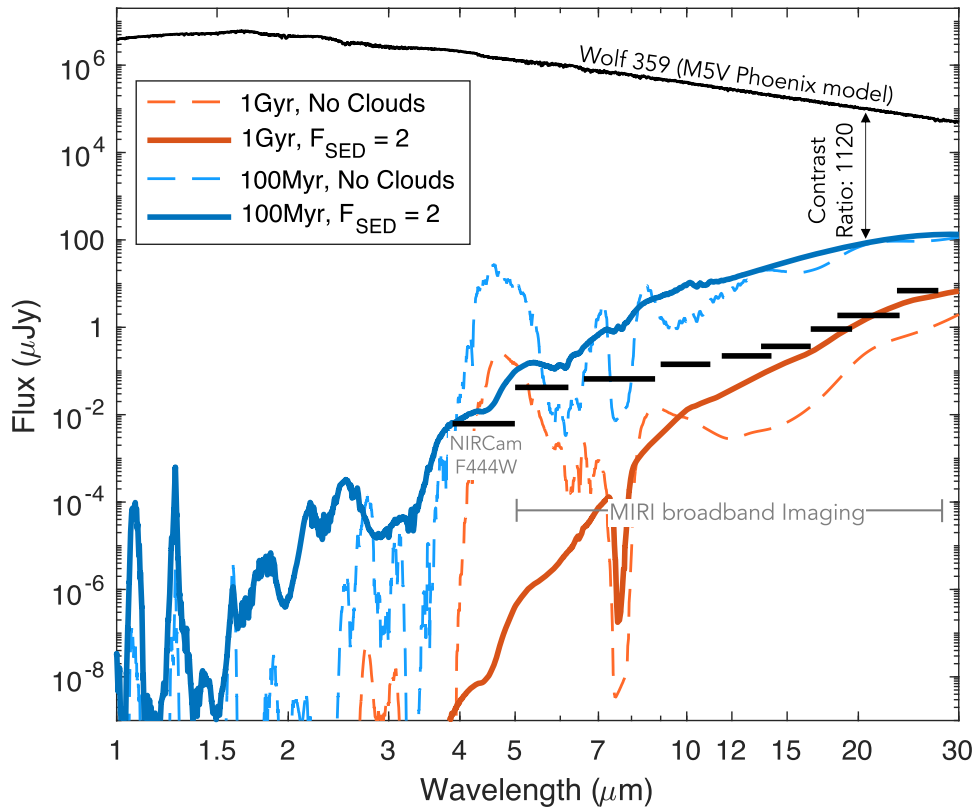


Figure 12. Emission from a cloudy (solid lines) and clear (dashed lines) sub-Saturn ($0.12 M_{\text{Jup}}$) at 100 Myr (blue) and 1 Gyr (red). The black line shows the emission from the star, Wolf 359, assuming an M5V spectral type. The black bars show the 3 hr, 5σ detection limits of NIRCcam F444W and MIRI broadband imaging. At $21 \mu\text{m}$, the contrast ratio between the star and a 100 Myr, $0.12 M_{\text{Jup}}$ exoplanet is only $1120\times$. For the older exoplanet, the contrast ratio is $15,800\times$.

In Figure 13, the shaded blue region above the black dashed line indicates the detectable exoplanet parameter space. With 3 hr of observation and using KLIP, a $0.12 M_{\text{Jup}}$ planet with an age of 100 Myr with moderate cloud cover would be detectable at separations greater than 1.5 au. With the same 3 hr integration time, an older (1 Gyr) exoplanet of this size would also be detectable at wider separations (>4 au). This approach requires an integration time that could fit into the JWST small proposals program and has the potential to detect nearby exoplanets to remarkably low masses.

5. Conclusions

We conducted a joint high-contrast imaging (HCI) and radial velocity (RV) survey with the goal of constraining long-period companions around the nearby M dwarf star Wolf 359. We do not rule out or confirm the Wolf 359 b RV candidate as presented by Tuomi et al. (2019).

To define the companion mass upper limits placed by our imaging search, we performed an updated age analysis of Wolf 359 through kinematic age dating, CMD young moving group comparisons, and a MIST stellar isochrone comparison. We draw a conclusion of relative youth from the star’s rotation period and adopt the kinematic age of 1.53 ± 0.3 Gyr as the upper bound for Wolf 359’s age. We rule out age estimates that are younger than 112 Myr through the comparison with young moving groups. Our MIST isochrone analysis produced an age estimate of 400 Myr.

We conducted an HCI survey using Keck-NIRC2 with the M_s filter ($4.67 \mu\text{m}$) in conjunction with the vector vortex coronagraph. We totaled 4.98 hr of integration time spread

Table 5
Summary of the NIRCcam F444W Coronagraphic Imaging Detectability of Cloudless Companions

Planet Mass	Age	Predicted Apparent F444W mag	Sep. Where Detectable by NIRCcam 1 hr ADI
$1 M_{\text{Jup}}$	100 Myr	12.90	>0.6 au
$1 M_{\text{Jup}}$	300 Myr	14.42	>0.8 au
$1 M_{\text{Jup}}$	500 Myr	15.19	>0.9 au
$1 M_{\text{Jup}}$	1200 Myr	17.05	>1.4 au
$1 M_{\text{Jup}}$	1500 Myr	17.34	>1.5 au
$0.5 M_{\text{Jup}}$	100 Myr	14.32	>0.8 au
$0.5 M_{\text{Jup}}$	300 Myr	16.09	>1.1 au
$0.5 M_{\text{Jup}}$	500 Myr	17.08	>1.4 au
$0.5 M_{\text{Jup}}$	1200 Myr	19.51	>3.7 au
$0.5 M_{\text{Jup}}$	1500 Myr	20.37	>4.7 au
$50 M_{\oplus}$	100 Myr	17.06	>1.4 au
$50 M_{\oplus}$	300 Myr	19.37	>3.6 au
$50 M_{\oplus}$	500 Myr	20.85	>5.7 au
$20 M_{\oplus}$	100 Myr	19.70	>3.9 au
$20 M_{\oplus}$	300 Myr	23.33	Not detectable

across 3 half-nights. The completeness of our imaging survey is highest (95%) for the semimajor axis range from 1 to 3 au. Our HCI results rule out a stellar or brown dwarf companion with this semimajor axis range to 5σ , and companions smaller than $0.4 M_{\text{Jup}}$ cannot be ruled out at any separation assuming an age older than 100 Myr. We compared our HCI survey’s predicted performance as estimated by the NIRC2 S/N calculator to our

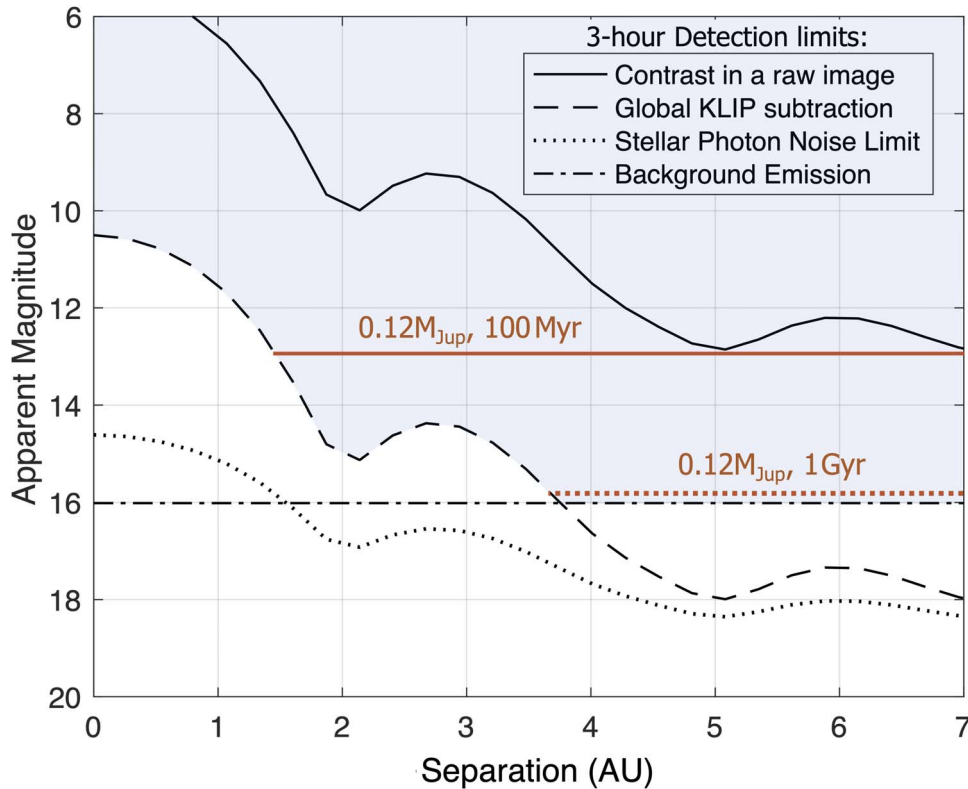


Figure 13. Simulated contrast curve for JWST broadband imaging at $21 \mu\text{m}$. The solid black line shows the contrast in the raw image, the dashed black line is the residual after KLIP (assuming it is possible to achieve performance comparable to Rajan et al. 2015), and the dotted black line shows the photon noise limit from stellar flux. The dashed–dotted black line shows the 5σ noise limit due to background emission. The shaded blue region above the KLIP contrast line and background emission line indicates the parameter space where it should be possible to detect exoplanets. The apparent magnitude of cloudy 100 Myr and 1 Gyr, $0.12 M_{\text{Jup}}$ exoplanets is shown by the red lines. This shows that a cloudy 100 Myr, $0.12 M_{\text{Jup}}$ exoplanet should be detectable at separations of >1.5 au, and a cloudy 1 Gyr, $0.12 M_{\text{Jup}}$ exoplanet is detectable at separations of >4 au. For this simulation, we assumed $[F2100W] = 5.3$ mag based on the star’s WISE band 4 ($\lambda = 22.2 \mu\text{m}$) magnitude.

measured 5σ performance and found a discrepancy of 1.7 mag for the night of 2021 March 31 (UT). This discrepancy can be partially accounted for by adjusting for the throughput loss when using the vortex at $4.7 \mu\text{m}$ and the fixhex pupil stop. Our analysis suggests that the remaining performance discrepancy may be due to the background noise exceeding the expected Poisson noise level over time, indicating that it may be possible to improve the sensitivity of future surveys using faster image readout to better compensate for changes in the sky background.

We performed an updated RV analysis of Wolf 359 with the `RVSearch` and `radvel` python packages with data from four RV instruments: CARMENES, HARPS, Keck-HIRES, and MAROON-X. After removing the known RV signal caused by the stellar rotation, we detect no signals above a false-alarm probability of 0.1%. To 2σ , we exclude planets with a minimum mass bigger than $m_p \sin i > 13.5 M_{\oplus}$ ($0.0425 M_{\text{Jup}}$) with a semimajor axis smaller than $a < 0.1$ au and $m_p \sin i > 147 M_{\oplus}$ ($0.46 M_{\text{Jup}}$) for a semimajor axis of less than $a < 1$ au.

We simulated JWST NIRCcam and MIRI observations to explore the potential of JWST to directly image ice giant and gas giant exoplanets orbiting Wolf 359. We predict that NIRCcam coronagraphic imaging could detect cloudless exoplanets with masses of $>1 M_{\text{Jup}}$ outside 1.5 au and $>0.5 M_{\text{Jup}}$ outside 4.7 au with 1 hr of integration time (assuming an age younger than <1.5 Gyr). Saturn- and Neptune-mass exoplanets are accessible to NIRCcam in certain age/separation spaces, and it is unlikely that NIRCcam could detect a sub-Neptune-mass exoplanet. While

MIRI imaging does not perform as well at smaller inner working angles, MIRI is capable of detecting cloudy exoplanets at smaller masses. We predict that a cloudy companion with a mass of $0.12 M_{\text{Jup}}$ could be directly imaged to 5σ if orbiting outside 4 au using 3 hr of integration time (assuming an age of younger than 1 Gyr).

This survey of Wolf 359 further establishes the methods needed to comprehensively characterize exoplanet systems using the intersection of multiple measurement techniques. As our future direct imaging instrumentation and RV surveys gain an increased sensitivity to ice giant exoplanets and super-Earths, the Wolf 359 system will continue to be a compelling target for understanding the cold planet population and planet formation outside the snow line of low-mass stars.

Acknowledgments

The authors wish to recognize and acknowledge the very significant cultural role and reverence that the summit of Maunakea has always had within the indigenous Hawaiian community. We are most fortunate to have the opportunity to conduct observations from this mountain.

R.B.R. would like to thank Mikko Tuomi and Ignasi Ribas for their collaboration to include the HARPS-TERRA and CARMENES radial velocity data products. R.B.R. also thanks Ester Linder, Jonathan Fortney, Andrew Skemer, Jorge Llop-Sayson, Andrew Howard, Caroline Morley, Kevin McKinnon, Kevin Wagner, Steve Ertl, Jason Wang, and Zack Breismeister for lending their scientific expertise. R.B.R. thanks Jules

Fowler for their endless sound-boarding, python help, and the title suggestion for this paper.

The authors would like to acknowledge the Keck staff who supported this observation, including the observing assistants, Arina Rostopchina and Julie Renaud-Kim, and the instrument scientists, Carlos Alvarez and Greg Doppmann. We thank Charlotte Bond and Sam Ragland, who supported the operation of the pyramid wave-front sensor, and the following observers for their contribution in collecting the HIRES velocities: Isabel Angelo, Corey Beard, Aida Behmard, Sarah Blunt, Fei Dai, Paul Dalba, Benjamin Fulton, Steven Giacalone, Rae Holcomb, Emma Loudon, Jack Lubin, Andrew Mayo, Daria Pidhorodetska, Alex Polanski, Malena Rice, Emma Turtelboom, Dakotah Tyler, Lauren Weiss, and Judah Van Zandt.

The data presented were obtained at the W. M. Keck Observatory, which is operated as a scientific partnership among the California Institute of Technology, the University of California, and the National Aeronautics and Space Administration. The Observatory was made possible by the financial support of the W. M. Keck Foundation.

The University of Chicago group acknowledges funding for the MAROON-X project from the David and Lucile Packard Foundation, the Heising-Simons Foundation, the Gordon and Betty Moore Foundation, the Gemini Observatory, the NSF (award No. 2108465), and NASA (grant No. 80NSSC22K0117). We thank the staff of the Gemini Observatory for their assistance with the commissioning and operation of the instrument. The Gemini observations are associated with programs GN-2021A-Q-119, GN-2021B-Q-122, and GN-2022A-Q-119.

G.S. acknowledges support provided by NASA through NASA Hubble Fellowship grant HST-HF2-51519.001-A awarded by the Space Telescope Science Institute, which is operated by the Association of Universities for Research in Astronomy, Inc., for NASA, under contract NAS5-26555.

J.M.A.M. is supported by the National Science Foundation (NSF) Graduate Research Fellowship Program under grant No. DGE-1842400. J.M.A.M. acknowledges the LSSTC Data Science Fellowship Program, which is funded by LSSTC, NSF Cybertraining grant No. 1829740, the Brinson Foundation, and

the Moore Foundation; his participation in the program has benefited this work.

Software: QACTIS IDL software package (Huby et al. 2017), VIP: Vortex Imaging Processing python package (Gomez Gonzalez et al. 2017), Species (Stolker et al. 2020), Exo-DMC (Bonavita 2020), RVSearch (Rosenthal et al. 2021), radvel (Fulton et al. 2018), PanCAKE (Girard et al. 2018; Perrin et al. 2018; Carter et al. 2021), Astropy (Astropy Collaboration et al. 2013, 2018, 2022).

Appendix A Supplemental RV Information

A sample of the RV measurements used to complete the RVSearch analysis is listed in Table 6. The full RV data set contains 275 velocities compiled from CARMENES, HARPS, Keck-HIRES, and MAROON-X. The measurements made by our MAROON-X and Keck-HIRES observations are available in Tables 7 and 8. The complete tables are available in machine-readable format online.

Table 6
Velocities Used in the RVSearch Analysis

Time (BJD-2,400,000)	RV (m s ⁻¹)	RV Unc. (m s ⁻¹)	Inst.
57,397.72509	-10.76	2.10	CARMENES
57,401.67629	6.00	1.18	CARMENES
57,419.56606	-11.86	1.32	CARMENES
57,444.58536	3.66	1.52	CARMENES
57,449.637	-1.18	1.61	CARMENES
...
59,688.83007	1.37	1.07	MAROONX _{red}
59,689.92024	-12.65	1.02	MAROONX _{red}
59,690.82035	-3.38	1.03	MAROONX _{red}
59,695.91704	-4.68	1.04	MAROONX _{red}
59,696.82571	-1.51	1.03	MAROONX _{red}

Note. The first five and last five velocities that were used in the RVSearch analysis are shown here as an example. HIRES_k and HIRES_j refer to Keck-HIRES observations made before and after the detector upgrade in 2004.

(This table is available in its entirety in machine-readable form.)

Table 7
RV Measurements for Observations Completed with Keck-HIRES

Time (UT)	BJD	RV (m s^{-1})	RV Unc. (m s^{-1})	cts	mdchi	bc (m s^{-1})	svalue	svalue _{err}	trv (km s^{-1})	trv _{err} (km s^{-1})
2019-02-18 09:53:43.341	2,458,532.912307	-28.3243	4.7225	1783.0	1.3819	7552.995	65.23	0.001	19.25	0.1
2019-03-17 07:57:58.734	2,458,559.83193	-20.5685	4.3440	1763.0	1.3092	-6334.391	59.76	0.001	18.96	0.1
2020-12-04 13:21:27.239	2,459,188.056565	6.8819	2.7510	5117.0	1.6743	30,511.618	49.17	0.001	18.97	0.1
2021-01-18 10:23:16.919	2,459,232.932835	-4.1504	3.9815	4845.0	1.6342	21,581.42	84.43	0.001	19.43	0.1
2021-02-23 08:01:42.226	2,459,268.834516	10.9828	3.2371	4871.0	1.6621	4894.409	69.74	0.001	19.31	0.1
2021-04-09 11:18:43.373	2,459,313.971335	-5.0129	3.1419	5088.0	1.6624	-17,770.269	67.85	0.001	-101.04	0.1
2021-06-14 07:33:53.169	2,459,379.815199	-10.2586	3.1191	4636.0	1.6224	-29,242.665	73.78	0.001	18.92	0.1
2021-06-24 07:15:16.741	2,459,389.802277	5.8263	3.1427	4664.0	1.6652	-27,939.286	108.0	0.001	18.68	0.1
2021-12-17 12:05:46.440	2,459,566.00401	3.7792	2.8511	4541.0	1.6260	29,791.676	61.49	0.001	19.2	0.1
2022-01-13 10:21:53.730	2,459,592.931872	-9.8209	3.8080	3774.0	1.5332	23,485.419	70.49	0.001	19.17	0.1
2022-02-21 08:31:28.284	2,459,631.855188	-11.4183	3.3142	4584.0	1.5754	6033.566	78.8	0.001	19.02	0.1
2022-02-22 09:08:41.970	2,459,632.881041	-0.4443	3.4243	4284.0	1.6415	5444.217	82.33	0.001	19.08	0.1

Note. cts—counts in raw ID spectrum near 5500 Å [e-]; chi—median-reduced χ^2 for the observation over all chunks; bc—barycentric velocity at flux-weighted midpoint [m s^{-1}]; svalue—CaHK S -value; svalue_{err}—CaHK S -value uncertainty; trv—telluric-calibrated absolute RV [km s^{-1}]; trv_{err}—uncertainty in telluric-calibrated absolute RV [km s^{-1}].

(This table is available in its entirety in machine-readable form.)

Table 8
RV Measurements for Observations Completed with MAROON-X

Arm	BJD	RV_po	e_RV_po	snpeak	exptime	berv	airmass	dLW	e_dLW	crx	e_crX	off. epoch	offset	e_offset	RV	e_rv
Blue	2,459,267.8235215	-14.64	1.35	66.0	1800	5.43	1.72	-7.79	1.87	-5.21	23.03	1	-1.5	0.5	-13.14	1.44
Blue	2,459,269.9620281	-8.71	0.94	81.0	1800	3.97	1.03	-16.21	1.29	-9.95	15.60	1	-1.5	0.5	-7.21	1.07
Blue	2,459,320.8841243	3.48	0.82	94.0	1800	-20.33	1.09	8.75	1.11	-1.58	11.83	2	0.0	0.0	3.48	0.82
Blue	2,459,321.8689137	-11.94	1.05	72.0	1800	-20.66	1.06	-30.50	1.45	-4.65	18.10	2	0.0	0.0	-11.94	1.05
Blue	2,459,322.9199499	-0.89	0.91	88.0	1800	-21.16	1.23	-29.97	1.26	2.13	15.72	2	0.0	0.0	-0.89	0.91
Blue	2,459,332.9311944	-6.96	1.27	71.0	1800	-24.44	1.51	-1.17	1.75	31.35	18.35	2	0.0	0.0	-6.96	1.27
Blue	2,459,333.8404301	-0.58	0.68	109.0	1800	-24.50	1.07	-34.30	0.93	23.86	10.83	2	0.0	0.0	-0.58	0.68
Blue	2,459,334.8384658	-10.13	0.68	108.0	1800	-24.78	1.07	-20.69	0.94	15.79	11.59	2	0.0	0.0	-10.13	0.68
Blue	2,459,359.8578599	-9.48	1.45	64.0	1800	-29.37	1.51	22.24	1.99	-14.84	22.69	3	2.5	1.5	-11.98	2.09
Blue	2,459,361.8234208	-12.07	0.86	99.0	1800	-29.45	1.29	-0.19	1.18	-12.82	13.34	3	2.5	1.5	-14.57	1.73
Blue	2,459,362.8356031	-3.80	1.17	82.0	1800	-29.53	1.39	5.57	1.61	-2.97	21.52	3	2.5	1.5	-6.30	1.90
Blue	2,459,363.8070943	5.54	0.84	101.0	1800	-29.52	1.23	9.00	1.15	45.59	12.53	3	2.5	1.5	3.04	1.72
Blue	2,459,364.8529316	-14.66	1.25	81.0	1800	-29.66	1.61	1.79	1.73	-33.41	37.31	3	2.5	1.5	-17.16	1.95
Blue	2,459,367.7719152	-9.82	0.88	94.0	1800	-29.58	1.13	-24.13	1.21	-8.87	9.92	3	2.5	1.5	-12.32	1.74
Blue	2,459,368.8130652	-1.22	0.89	97.0	1800	-29.68	1.34	-14.78	1.23	10.27	10.50	3	2.5	1.5	-3.72	1.74
Blue	2,459,515.1284389	7.45	1.54	66.0	1800	24.07	2.03	14.83	2.13	-26.51	27.23	4	8.0	1.0	-0.55	1.83
Blue	2,459,518.140394	8.22	1.24	71.0	1800	24.98	1.69	27.88	1.70	-17.33	17.08	4	8.0	1.0	0.22	1.59
Blue	2,459,525.1065205	-5.89	1.60	58.0	1800	26.94	1.92	15.17	2.21	-8.92	27.06	4	8.0	1.0	-13.89	1.89
Blue	2,459,527.1188207	4.16	1.03	86.0	1800	27.40	1.65	8.78	1.42	10.32	14.81	4	8.0	1.0	-3.84	1.44
Blue	2,459,530.1308991	4.48	0.81	104.0	1800	28.02	1.44	-1.47	1.12	13.60	12.24	4	8.0	1.0	-3.52	1.29
Blue	2,459,539.1271668	0.46	0.95	84.0	1800	29.49	1.28	-1.42	1.31	2.73	9.44	4	8.0	1.0	-7.54	1.38
Blue	2,459,540.1210453	1.26	0.77	108.0	1800	29.62	1.31	-8.13	1.05	-0.08	9.74	4	8.0	1.0	-6.74	1.26
Blue	2,459,541.1118372	-2.48	0.79	105.0	1800	29.75	1.35	1.00	1.08	-9.11	10.39	4	8.0	1.0	-10.48	1.27
Blue	2,459,666.8346899	5.59	0.62	118.0	1800	-11.91	1.07	-12.53	0.84	12.81	7.19	5	11.0	1.0	-5.41	1.17
Blue	2,459,677.8746489	4.58	0.87	85.0	1800	-17.01	1.04	-11.46	1.19	3.43	10.10	5	11.0	1.0	-6.42	1.32
Blue	2,459,678.8934433	-1.64	1.03	72.0	1800	-17.49	1.06	-7.99	1.42	-1.25	12.33	5	11.0	1.0	-12.64	1.43
Blue	2,459,680.8488688	11.42	0.98	75.0	1800	-18.17	1.03	13.24	1.34	13.21	12.82	5	11.0	1.0	0.42	1.40
Blue	2,459,683.8770181	9.33	0.63	116.0	1800	-19.44	1.06	42.70	0.84	13.57	7.16	5	11.0	1.0	-1.67	1.18
Blue	2,459,684.9261998	-1.01	0.61	113.0	1800	-19.96	1.22	10.71	0.83	-4.58	7.21	5	11.0	1.0	-12.01	1.17
Blue	2,459,688.830072	11.27	1.59	48.0	1800	-21.16	1.03	18.41	2.17	13.31	19.52	5	11.0	1.0	0.27	1.88
Blue	2,459,689.9202404	-5.46	0.57	121.0	1800	-21.77	1.26	-11.84	0.78	-8.66	7.88	5	11.0	1.0	-16.46	1.15
Blue	2,459,690.820352	6.56	0.63	111.0	1800	-21.84	1.03	-21.48	0.87	12.18	8.73	5	11.0	1.0	-4.44	1.18
Blue	2,459,695.9170363	7.44	0.94	81.0	1800	-23.75	1.35	17.30	1.28	8.29	13.65	5	11.0	1.0	-3.56	1.37
Blue	2,459,696.8257078	6.11	0.98	110.0	1800	-23.82	1.04	127.82	1.22	25.24	12.37	5	11.0	1.0	-4.89	1.40
Red	2,459,267.8235215	-16.62	0.39	375.0	1800	5.43	1.72	60.96	0.45	29.81	7.62	1	-1.6	0.5	-15.02	0.63
Red	2,459,269.9620281	-9.27	0.38	403.0	1800	3.97	1.03	65.80	0.43	0.20	6.09	1	-1.6	0.5	-7.67	0.63
Red	2,459,320.8841243	-0.58	0.34	468.0	1800	-20.33	1.09	71.81	0.37	-22.98	4.82	2	0.0	0.0	-0.58	0.34
Red	2,459,321.8689137	-10.45	0.34	365.0	1800	-20.66	1.06	55.56	0.41	13.75	6.07	2	0.0	0.0	-10.45	0.34
Red	2,459,322.9199499	-1.93	0.30	461.0	1800	-21.16	1.23	55.41	0.34	0.01	3.79	2	0.0	0.0	-1.93	0.30
Red	2,459,332.9311944	-4.96	0.32	419.0	1800	-24.44	1.51	54.08	0.38	12.32	4.48	2	0.0	0.0	-4.96	0.32
Red	2,459,333.8404301	0.65	0.30	531.0	1800	-24.50	1.07	55.95	0.34	-5.79	3.50	2	0.0	0.0	0.65	0.30
Red	2,459,334.8384658	-11.28	0.31	529.0	1800	-24.78	1.07	63.81	0.34	25.58	6.89	2	0.0	0.0	-11.28	0.31
Red	2,459,359.8578599	-4.78	0.28	379.0	1800	-29.37	1.51	-21.86	0.38	10.07	4.68	3	2.2	1.0	-6.98	1.04
Red	2,459,361.8234208	-9.22	0.23	519.0	1800	-29.45	1.29	-18.08	0.31	14.87	4.46	3	2.2	1.0	-11.42	1.03
Red	2,459,362.8356031	-2.32	0.23	483.0	1800	-29.53	1.39	-22.59	0.31	0.39	3.41	3	2.2	1.0	-4.52	1.03
Red	2,459,363.8070943	4.11	0.23	523.0	1800	-29.52	1.23	-9.55	0.31	-33.92	5.02	3	2.2	1.0	1.91	1.03
Red	2,459,364.8529316	-10.04	0.22	539.0	1800	-29.66	1.61	-22.92	0.29	19.62	5.67	3	2.2	1.0	-12.24	1.02
Red	2,459,367.7719152	-7.97	0.23	487.0	1800	-29.58	1.13	-25.37	0.30	9.56	4.71	3	2.2	1.0	-10.17	1.03

Table 8
(Continued)

Arm	BJD	RV_po	e_RV_po	snpeak	exptime	berv	airmass	dLW	e_dLW	crx	e_crx	off. epoch	offset	e_offset	RV	e_rv
Red	2,459,368.8130652	2.06	0.23	519.0	1800	-29.68	1.34	-20.19	0.30	-15.18	4.62	3	2.2	1.0	-0.14	1.03
Red	2,459,515.1284389	4.52	0.30	417.0	1800	24.07	2.03	-24.05	0.40	-11.83	5.67	4	7.0	1.0	-2.48	1.04
Red	2,459,518.140394	3.98	0.30	389.0	1800	24.98	1.69	-17.33	0.41	-18.53	5.24	4	7.0	1.0	-3.02	1.04
Red	2,459,525.1065205	-4.96	0.33	334.0	1800	26.94	1.92	-19.60	0.46	22.67	7.77	4	7.0	1.0	-11.96	1.05
Red	2,459,527.1188207	4.37	0.26	470.0	1800	27.40	1.65	-19.71	0.35	-10.88	4.60	4	7.0	1.0	-2.63	1.03
Red	2,459,530.1308991	2.87	0.24	537.0	1800	28.02	1.44	-21.33	0.32	-9.00	3.84	4	7.0	1.0	-4.13	1.03
Red	2,459,539.1271668	0.86	0.29	427.0	1800	29.49	1.28	-27.30	0.38	12.48	4.96	4	7.0	1.0	-6.14	1.04
Red	2,459,540.1210453	2.55	0.25	543.0	1800	29.62	1.31	-26.80	0.32	4.92	3.75	4	7.0	1.0	-4.45	1.03
Red	2,459,541.1118372	0.06	0.24	531.0	1800	29.75	1.35	-20.85	0.32	9.26	3.13	4	7.0	1.0	-6.94	1.03
Red	2,459,666.8346899	8.39	0.23	565.0	1800	-11.91	1.07	-28.82	0.29	0.66	3.68	5	10.0	1.0	-1.61	1.03
Red	2,459,677.8746489	6.42	0.27	416.0	1800	-17.01	1.04	-30.48	0.35	-6.16	4.43	5	10.0	1.0	-3.58	1.04
Red	2,459,678.8934433	0.88	0.29	362.0	1800	-17.49	1.06	-26.49	0.38	7.39	5.50	5	10.0	1.0	-9.12	1.04
Red	2,459,680.8488688	9.62	0.28	374.0	1800	-18.17	1.03	-24.81	0.38	-21.12	4.33	5	10.0	1.0	-0.38	1.04
Red	2,459,683.8770181	8.59	0.21	550.0	1800	-19.44	1.06	-19.94	0.27	-14.60	3.76	5	10.0	1.0	-1.41	1.02
Red	2,459,684.9261998	1.28	0.23	539.0	1800	-19.96	1.22	-26.99	0.29	5.97	3.37	5	10.0	1.0	-8.72	1.03
Red	2,459,688.830072	11.37	0.39	242.0	1800	-21.16	1.03	-27.16	0.53	-19.19	5.03	5	10.0	1.0	1.37	1.07
Red	2,459,689.9202404	-2.65	0.22	580.0	1800	-21.77	1.26	-27.18	0.28	25.49	4.46	5	10.0	1.0	-12.65	1.02
Red	2,459,690.820352	6.62	0.24	527.0	1800	-21.84	1.03	-29.38	0.30	-7.89	3.67	5	10.0	1.0	-3.38	1.03
Red	2,459,695.9170363	5.32	0.28	399.0	1800	-23.75	1.35	-25.53	0.37	0.19	3.56	5	10.0	1.0	-4.68	1.04
Red	2,459,696.8257078	8.49	0.24	515.0	1800	-23.82	1.04	-11.83	0.33	-10.49	5.78	5	10.0	1.0	-1.51	1.03

Note. BJD—Julian Date [days]; rv_po/e_rv_po—barycentric-corrected RV (and its error) pre-offset correction by observing run epoch [m s^{-1}]; sn_peak—peak S/N in observation; exptime—exposure time [s]; berv—flux-weighted barycentric correction included in final velocities, standard barycentric correction to RV [m s^{-1}]; airmass—observation airmass; dLW/e_dLW—differential linewidth of observation (an activity indicator described in the serval documentation) [$1000 \text{ m}^2 \text{ s}^{-2}$]; crx/e_crx—chromatic index of observation (an activity indicator described in the serval documentation) [$\text{m s}^{-1}/\text{Np}$]; irt_ind/e_irt_ind—CaIRT indices of observation; off. epoch—observing run epoch with an applicable instrument offset [m s^{-1}]; offset/e_offset—RV offset measured between observing runs [m s^{-1}]; rv/e_rv—barycentric- and offset-corrected by observing epoch RV (and its error) [m s^{-1}].

(This table is available in machine-readable form.)

Appendix B

Revised S/N Estimations for Keck-NIRC2 with the Vortex Coronagraph in the *M* Band

The W. M. Keck Observatory provides an online tool to help observers plan their NIRC2 observations: the NIRC2 S/N and efficiency calculator (see footnote 21). The NIRC2 calculator does not provide performance estimates for using the vector vortex coronagraph mask, which is a common configuration for conducting HCI observations to hunt for exoplanet and brown dwarf companions. In this section, we offer a method to modify the equations used by the NIRC2 calculator to aid in the S/N prediction when using the *L/M*-band vortex (Serabyn et al. 2017) with the *Ms* filter.

We recommend that observers planning to use the *Lp* filter in conjunction with the *L/M*-band vortex use the Vortex Imaging Contrast Oracle (VICO²⁵; Xuan et al. 2018) instead of the equations documented here. VICO produces a full contrast curve based on user inputs for the host’s magnitude, the survey’s total integration time, and the predicted spanned parallactic angle. VICO’s performance and contrast predictions are based on a training set of 304 targets that were observed between 2015 and 2018 using the Shack–Hartmann wave-front sensor to perform AO correction.

We consider S/N predictions only and do not attempt to match the efficiency predictions made by the NIRC2 calculator. The predictions offered by our modified equations are intended to predict the S/N in the background-limited regions, where light from the host star is negligible in comparison to the background flux. We do not attempt to predict the full contrast curve or the S/N in the speckle-limited regions of the image.

Table 9 shows the values defined internally to the NIRC2 S/N calculator alongside our choices for the user-defined parameters that are applicable to our observing mode. The calculator internally defines the read noise, gain, zero-point for each filter, and number of pixels within an FWHM for each filter. The user is able to specify the object magnitude, Strehl ratio, time per exposure (tint), coadds, number of dithers, repeats per dither, camera mode (narrow versus wide), filter, number of reads, array window size, and AO mode (natural guide star versus laser guide star). We matched our user-defined parameters to our 2021 March 31 (UT) data set to compare the predicted performance to the measured performance on that night. Terms related to laser motion control were excluded because our observations were performed using natural guide star AO. We adopted a Strehl ratio of 0.85 for our predictions, which is a conservative estimate equivalent to 300 nm of error on the wave front.

We began the modifications to the equations used in the NIRC2 S/N calculator by adding a corrective factor for the throughput for using Keck II’s fixedhex pupil stop. The NIRC2 S/N calculator assumes that NIRC2 images will be taken with Keck Observatory’s circular largehex pupil stop. However, when operating NIRC2 in conjunction with the vortex coronagraph, the fixedhex pupil is typically used. The fixedhex pupil was specifically tailored for use with the vortex coronagraph at Keck, and its shape blocks the telescope’s spiders and central obscuration. It has a throughput of 84% as compared to the largehex pupil. We assigned a 0.84 throughput penalty for this difference in pupil stop.

We further refined our throughput penalty by accounting for the throughput hit due to the absorption by the vector vortex coronagraph at 4.67 μm . The throughput of the Keck annular groove phase mask was measured in the lab to be $70\% \pm 3\%$ (Jolivet et al. 2019, AGPM-L9r2 in Table 4). We conducted on-sky testing to verify this throughput as observed with the full optical system in 2022 June. We imaged HIP 74785 using the fixhexed pupil for all images. We moved the vortex coronagraph in and out of the optical path to create a direct comparison to measure the transmission of the vortex mask. When the vortex was in place, it was intentionally miscentered with respect to the stellar PSF to ensure that no flux from the star was blocked due to the coronagraphy properties of the vortex. The stellar photometry was then measured in each image using `photutils` within a circular aperture of 60 pixels in radius. The throughput ratio of the no-vortex to with-vortex stellar flux was measured to be $68\% \pm 3\%$. While the vortex throughput measurement using on-sky images is consistent with laboratory tests, we note that we find that there was a slight defocus in the on-sky images when the vortex was in place, such that a photometry aperture radius of >5 FWHM needed to be used to achieve this consistency.

We document both the lab and on-sky testing values for the throughput penalty due to the vortex absorption in Table 9 alongside our calculation for the total throughput penalty. The total throughput penalty was calculated by multiplying the vortex throughput penalty by the fixhex throughput penalty. We adopted the more pessimistic value of the total throughput penalty (57%) when discussing the performance of NIRC2 in Section 4.

To quantify a correction factor for the background flux, we measured the background flux per pixel in each image for our full data cube from the 3 observing nights of Wolf 359. The NIRC2 calculator assumes a value of $18,535 \text{ DN s}^{-1} \text{ pixel}^{-1}$ for the sky background contribution when observing in narrow mode with the *Ms* filter using no vortex with the largehex pupil. We measured the sky background in our images with the vortex and fixhex pupil by finding the median of each image cube. We then averaged those medians by night to find an average image median of $17,457 \pm 4 \text{ DN s}^{-1}$ on 2021 February 22, $17,008 \pm 7 \text{ DN s}^{-1}$ on 2021 February 23, and $17,850 \pm 106 \text{ DN s}^{-1}$ on 2021 March 31. These values indicate that there is a measurable excess background flux when the vortex optic is in place, as the background counts do not scale with the throughput penalty. We adopt the most pessimistic value for the background flux (2021 March 31) for our discussion of the NIRC2 performance in Section 4.

The equations outlined in this appendix account for the throughput penalty of using the vortex only. When applied to the Wolf 359 2021 March 31 data set, this method of prediction overestimated the 5σ performance capabilities by ~ 1 mag. We caution observers who are planning to detect a companion dimmer than $m_s = 14.4$ with Keck-NIRC2 using one or more half-nights to approach the observation carefully and not rely solely on the online NIRC S/N calculator or the equations listed in this section.

Equations to calculate the S/N. The terms that deviate from the formulae used by the NIRC2 S/N calculator are highlighted in red.

²⁵ <https://wxuan.shinyapps.io/contrast-oracle/>

$n_{\text{exp}} = \text{coadds} * n_{\text{images}}$	We assume no dithering
$m_{\text{zero}} = \text{zero-point} + 2.5 * \log_{10}(\text{Strehl})$	
$\text{bg} = \text{background} * \text{gain}$	Meas. background = 17,850 DN s ⁻¹ pixel ⁻¹
ThroughputPenalty = FixhexThroughput * VortexThroughput	Meas. ThroughputPenalty = 0.58
signal = ThroughputPenalty * $n_{\text{exp}} * \text{tint} * 10^{(0.4(m_{\text{zero}} - \text{mag}))}$	Signal after throughput penalty applied
$\sigma_{\text{read}}^2 = n_{\text{exp}} * r_{\text{noise}}^2 * n_{\text{pix}}$	Read noise
$\sigma_{\text{skybg}}^2 = n_{\text{pix}} * \text{bg} * n_{\text{exp}} * \text{tint}$	Photon-noise of sky background
$\sigma_{\text{photon}}^2 = \text{signal}$	Photon-noise of source
$\sigma_{\text{tot}} = \sqrt{\sigma_{\text{read}}^2 + \sigma_{\text{skybg}}^2 + \sigma_{\text{photon}}^2}$	Total noise
S/N = signal/ σ_{tot}	Signal-to-Noise

Table 9
Parameters Used in the Modified NIRC2 Performance Calculation

Parameter	Value	How Defined?	Notes
Read noise in electrons (r_{noise})	56	Internal	
Gain in e- per DN (gain)	4	Internal	
Zero-point for M_s filter in narrow mode (zero-point)	22.7	Internal	
Number of pixels in aperture (n_{pix})	490.8	Internal	
N reads	2 (CDS)	User	Two reads is a standard readout mode
Array window size	512	User	512 × 512 is a standard image size for HCI imaging
AO mode	NGS	User	Natural guide star mode
Strehl	0.85	User	Conservative assumption assuming 300 nm of wave-front error
Tint	0.3 s	User	Time per frame before coadd used in this survey
Coadds	90	User	No. of frames added together before a full read used in this survey
Number of images (n_{exp})	269	User	No. of images collected on 2021 Mar 31 of this survey
Fixhex throughput as compared to largehex pupil	0.84	Calculated	Ratio of the size of the fixedhex/largehex pupil at Keck
Vortex throughput at 4.6 μm meas. in lab	0.70 ± 0.03	Measured	AGPM-L9r2 in Table 4 of Jolivét et al. (2019)
Vortex throughput at 4.6 μm meas. on sky	0.68 ± 0.03	Measured	Meas. using data shared by Keck Obs. staff
Throughput penalty using vortex value meas. in lab	0.59 ± 0.03	Calculated	FixhexThrough * VortexThroughput _{lab}
Throughput penalty using vortex value meas. on sky	0.57 ± 0.03	Calculated	FixhexThrough * VortexThroughput _{sky} ; value adopted for NIRC2 performance discussion in Section 4
Background flux using vortex with fixhex pupil at 4.6 μm	$17,850 \text{ DN s}^{-1}$	Measured	Average DN s ⁻¹ meas. on 2021 Mar 31 of this survey

ORCID iDs

Rachel Bowens-Rubin  <https://orcid.org/0000-0001-5831-9530>
 Joseph M. Akana Murphy  <https://orcid.org/0000-0001-8898-8284>
 Philip M. Hinz  <https://orcid.org/0000-0002-1954-4564>
 Mary Anne Limbach  <https://orcid.org/0000-0002-9521-9798>
 Andreas Seifahrt  <https://orcid.org/0000-0003-4526-3747>
 Rocío Kiman  <https://orcid.org/0000-0003-2102-3159>
 Maïssa Salama  <https://orcid.org/0000-0002-5082-6332>
 Sagnick Mukherjee  <https://orcid.org/0000-0003-1622-1302>
 Madison Brady  <https://orcid.org/0000-0003-2404-2427>
 Aarynn L. Carter  <https://orcid.org/0000-0001-5365-4815>
 Rebecca Jensen-Clem  <https://orcid.org/0000-0003-0054-2953>

Maaïke A. M. van Kooten  <https://orcid.org/0000-0002-9805-3666>
 Howard Isaacson  <https://orcid.org/0000-0002-0531-1073>
 Molly Kosiarek  <https://orcid.org/0000-0002-6115-4359>
 Jacob L. Bean  <https://orcid.org/0000-0003-4733-6532>
 David Kasper  <https://orcid.org/0000-0003-0534-6388>
 Rafael Luque  <https://orcid.org/0000-0002-4671-2957>
 Gudmundur Stefánsson  <https://orcid.org/0000-0001-7409-5688>
 Julian Stürmer  <https://orcid.org/0000-0002-4410-4712>

References

Amara, A., & Quanz, S. P. 2012, *MNRAS*, 427, 948
 Anglada-Escudé, G., & Butler, R. P. 2012, *ApJS*, 200, 15
 Angus, R., Morton, T. D., Foreman-Mackey, D., et al. 2019, *AJ*, 158, 173
 Astropy Collaboration, Price-Whelan, A. M., Lim, P. L., et al. 2022, *ApJ*, 935, 167

- Astropy Collaboration, Price-Whelan, A. M., Sipőcz, B. M., et al. 2018, *AJ*, **156**, 123
- Astropy Collaboration, Robitaille, T. P., Tollerud, E. J., et al. 2013, *A&A*, **558**, A33
- Baraffe, I., Chabrier, G., Barman, T. S., Allard, F., & Hauschildt, P. H. 2003, *A&A*, **402**, 701
- Baraffe, I., Homeier, D., Allard, F., & Chabrier, G. 2015, *A&A*, **577**, A42
- Barnes, S. A., & Kim, Y.-C. 2010, *ApJ*, **721**, 675
- Batalha, N. E., Marley, M. S., Lewis, N. K., & Fortney, J. J. 2019, *ApJ*, **878**, 70
- Bessell, M. S. 2005, *ARA&A*, **43**, 293
- Bonavita, M., 2020 Exo-DMC: Exoplanet Detection Map Calculator, Astrophysics Source Code Library, ascl:2010.008
- Bond, C. Z., Cetre, S., Lilliey, S., et al. 2020, *JATIS*, **6**, 039003
- Bovy, J. 2015, *ApJS*, **216**, 29
- Brandner, W., Calissendorff, P., & Kopytova, T. 2023, *MNRAS*, **518**, 662
- Brandt, T. D. 2021, *ApJS*, **254**, 42
- Butler, R. P., Marcy, G. W., Williams, E., et al. 1996, *PASP*, **108**, 500
- Carter, A. L., Hinkley, S., Kammerer, J., et al. 2023, *ApJL*, **951**, L20
- Carter, A. L., Skemer, A. J. I., Danielski, C., et al. 2021, *Proc. SPIE*, **11823**, 118230H
- Cassan, A., Kubas, D., Beaulieu, J. P., et al. 2012, *Natur*, **481**, 167
- Chabrier, G., Baraffe, I., Allard, F., & Hauschildt, P. 2000, *ApJ*, **542**, 464
- Cheetham, A., Ségransan, D., Peretti, S., et al. 2018, *A&A*, **614**, A16
- Choi, J., Dotter, A., Conroy, C., et al. 2016, *ApJ*, **823**, 102
- Crepp, J. R., Gonzales, E. J., Bechter, E. B., et al. 2016, *ApJ*, **831**, 136
- Crepp, J. R., Gonzales, E. J., Bowler, B. P., et al. 2018, *ApJ*, **864**, 42
- Curtis, J. L., Agüeros, M. A., Matt, S. P., et al. 2020, *ApJ*, **904**, 140
- Cutri, R. M., Skrutskie, M. F., van Dyk, S., et al. 2003, *yCat*, **II/246**
- Dalba, P. A., Fulton, B., Isaacson, H., Kane, S. R., & Howard, A. W. 2020, *AJ*, **160**, 149
- Dotter, A. 2016, *ApJS*, **222**, 8
- Dunee, G., van Saders, J., Gaidos, E., et al. 2022, *ApJ*, **938**, 118
- Engle, S. G., & Guinan, E. F. 2018, *RNAAS*, **2**, 34
- Fernandes, R. B., Mulders, G. D., Pascucci, I., Mordasini, C., & Emsenhuber, A. 2019, *ApJ*, **874**, 81
- Fuhrmeister, B., Schmitt, J. H. M. M., & Hauschildt, P. H. 2005, *A&A*, **439**, 1137
- Fulton, B. J., Petigura, E. A., Blunt, S., & Sinukoff, E. 2018, *PASP*, **130**, 044504
- Gaia Collaboration, Brown, A. G. A., Vallenari, A., et al. 2021, *A&A*, **649**, A1
- Gaia Collaboration, Vallenari, A., Brown, A. G. A., et al. 2023, *A&A*, **674**, A1
- Gagné, J., Faherty, J. K., Moranta, L., & Popinchalk, M. 2021, *ApJL*, **915**, L29
- Gentile Fusillo, N. P., Tremblay, P. E., Cukanovaite, E., et al. 2021, *MNRAS*, **508**, 3877
- Girard, J. H., Blair, W., Brooks, B., et al. 2018, *Proc. SPIE*, **10698**, 106983V
- Gomez Gonzalez, C. A., Wertz, O., Absil, O., et al. 2017, *AJ*, **154**, 7
- Guinan, E. F., & Engle, S. G. 2018, *RNAAS*, **2**, 1
- Hinkley, S., Lacour, S., Marleau, G. D., et al. 2023, *A&A*, **671**, L5
- Howard, A. W., Johnson, J. A., Marcy, G. W., et al. 2010, *ApJ*, **721**, 1467
- Howell, S. B., Sobeck, C., Haas, M., et al. 2014, *PASP*, **126**, 398
- Huby, E., Bottom, M., Femenia, B., et al. 2017, *A&A*, **600**, A46
- Hunziker, S., Quanz, S. P., Amara, A., & Meyer, M. R. 2018, *A&A*, **611**, A23
- Husser, T. O., Wende-von Berg, S., Dreizler, S., et al. 2013, *A&A*, **553**, A6
- Irwin, J., Berta, Z. K., Burke, C. J., et al. 2011, *ApJ*, **727**, 56
- Jolivet, A., Orban de Xivry, G., Huby, E., et al. 2019, *JATIS*, **5**, 025001
- Kesseli, A. Y., Kirkpatrick, J. D., Fajardo-Acosta, S. B., et al. 2019, *AJ*, **157**, 63
- Kimman, R., Schmidt, S. J., Angus, R., et al. 2019, *AJ*, **157**, 231
- Kimman, R., Xu, S., Faherty, J. K., et al. 2022, *AJ*, **164**, 62
- Lafarga, M., Ribas, I., Reiners, A., et al. 2021, *A&A*, **652**, A28
- Landolt, A. U. 2009, *AJ*, **137**, 4186
- Leggett, S. K., Burningham, B., Saumon, D., et al. 2010, *ApJ*, **710**, 1627
- Limbach, M. A., Vanderburg, A., Stevenson, K. B., et al. 2022, *MNRAS*, **517**, 2622
- Lin, C.-L., Chen, W.-P., Ip, W.-H., et al. 2021, *AJ*, **162**, 11
- Lin, H.-T., Chen, W.-P., Liu, J., et al. 2022, *AJ*, **163**, 164
- Linder, E. F., Mordasini, C., Mollière, P., et al. 2019, *A&A*, **623**, A85
- Llop-Sayson, J., Wang, J. J., Ruffio, J.-B., et al. 2021, *AJ*, **162**, 181
- Lu, Y. L., Angus, R., Curtis, J. L., David, T. J., & Kiman, R. 2021, *AJ*, **161**, 189
- Mann, A. W., Feiden, G. A., Gaidos, E., Boyajian, T., & von Braun, K. 2015, *ApJ*, **804**, 64
- Mawet, D., Hirsch, L., Lee, E. J., et al. 2019, *AJ*, **157**, 33
- Mayor, M., Pepe, F., Queloz, D., et al. 2003, *Msngr*, **114**, 20
- Medina, A. A., Winters, J. G., Irwin, J. M., & Charbonneau, D. 2022, *ApJ*, **935**, 104
- Mukherjee, S., Batalha, N. E., Fortney, J. J., & Marley, M. S. 2023, *ApJ*, **942**, 71
- Mulders, G. D., Ciesla, F. J., Min, M., & Pascucci, I. 2015, *ApJ*, **807**, 9
- Newton, E. R., Irwin, J., Charbonneau, D., et al. 2017, *ApJ*, **834**, 85
- Newton, E. R., Mondrik, N., Irwin, J., Winters, J. G., & Charbonneau, D. 2018, *AJ*, **156**, 217
- Pass, E. K., Charbonneau, D., Irwin, J. M., & Winters, J. G. 2022, *ApJ*, **936**, 109
- Pavlenko, Y. V., Jones, H. R. A., Lyubchik, Y., Tennyson, J., & Pinfield, D. J. 2006, *A&A*, **447**, 709
- Pepe, F., Mayor, M., Rupprecht, G., et al. 2002, *Msngr*, **110**, 9
- Perrin, M. D., Pueyo, L., Van Gorkom, K., et al. 2018, *Proc. SPIE*, **10698**, 1069809
- Pineda, J. S., Youngblood, A., & France, K. 2021, *ApJ*, **918**, 40
- Poleski, R., Skowron, J., Mróz, P., et al. 2021, *AcA*, **71**, 1
- Popinchalk, M., Faherty, J. K., Kiman, R., et al. 2021, *ApJ*, **916**, 77
- Quirrenbach, A., Amado, P. J., Caballero, J. A., et al. 2016, *Proc. SPIE*, **9908**, 990812
- Rajan, A., Barman, T., Soummer, R., et al. 2015, *ApJL*, **809**, L33
- Ribas, I., Reiners, A., Zechmeister, M., et al. 2023, *A&A*, **670**, A139
- Rickman, E. L., Ségransan, D., Marmier, M., et al. 2019, *A&A*, **625**, A71
- Rieke, M. J., Kelly, D. M., Misselt, K., et al. 2023, *PASP*, **135**, 028001
- Rosenthal, L. J., Fulton, B. J., Hirsch, L. A., et al. 2021, *ApJS*, **255**, 8
- Seifahrt, A., Bean, J. L., Kasper, D., et al. 2022, *Proc. SPIE*, **12184**, 121841G
- Seifahrt, A., Bean, J. L., Stürmer, J., et al. 2020, *Proc. SPIE*, **11447**, 114471F
- Serabyn, E., Huby, E., Matthews, K., et al. 2017, *AJ*, **153**, 43
- Skumanich, A. 1972, *ApJ*, **171**, 565
- Soummer, R., Pueyo, L., & Larkin, J. 2012, *ApJL*, **755**, L28
- Stolker, T., Quanz, S. P., Todorov, K. O., et al. 2020, *A&A*, **635**, A182
- Suzuki, D., Bennett, D. P., Sumi, T., et al. 2016, *ApJ*, **833**, 145
- Trifonov, T., Caballero, J. A., Morales, J. C., et al. 2021, *Sci*, **371**, 1038
- Trifonov, T., Tal-Or, L., Zechmeister, M., et al. 2020, *A&A*, **636**, A74
- Tuomi, M., Jones, H. R. A., Butler, R. P., et al. 2019, arXiv:1906.04644
- Udry, S., Mayor, M., Naef, D., et al. 2000, *A&A*, **356**, 590
- Vogt, S. S., Allen, S. L., Bigelow, B. C., et al. 1994, *Proc. SPIE*, **2198**, 362
- Wagner, K., Boehle, A., Pathak, P., et al. 2021, *NatCo*, **12**, 922
- Wizinowich, P., Acton, D. S., Shelton, C., et al. 2000, *PASP*, **112**, 315
- Wright, G. S., Rieke, G. H., Glaspe, A., et al. 2023, *PASP*, **135**, 048003
- Wright, N. J., Drake, J. J., Mamajek, E. E., & Henry, G. W. 2011, *ApJ*, **743**, 48
- Xuan, W. J., Mawet, D., Ngo, H., et al. 2018, *AJ*, **156**, 156
- Yu, J., & Liu, C. 2018, *MNRAS*, **475**, 1093
- Zechmeister, M., Reiners, A., Amado, P. J., et al. 2018, *A&A*, **609**, A12